Supercritical electrostatic shocks in laboratory plasma

Contact *hahmed02@qub.ac.uk*

H.Ahmed, D.Doria, M.E.Dieckman, E.Ianni, G. Sarri, R. Prasad, K. Quinn, I. Kourakis and M. Borghesi

Centre for Plasma Physics, Queen's University Belfast, Belfast, BT7 1NN, U.K

L. Romagnani

LULI, École Polytechnique, CNRS, CEA, UPMC, route de Saclay, 91128 Palaiseau, France

M.Cerchez, A.L.Giesecke, O.Willi

Institute for Laser and Plasma Physics, university of Düsseldorf, Germany

Introduction

Electrostatic collisionless shocks (ECS) are relevant to many astrophysical scenarios [1], such as the generation of highly energetic particles and cosmic rays during supernova explosions, and have recently been the focus of several laboratory plasma investigations employing high-power lasers [2]. Intense laser plasma interaction provides a possible way to launch shock waves in conditions of relevance to space plasma, and recently collisionless shocks have been observed in a number of laser plasma scenarios [4,5,6].

The interaction of an intense laser pulse with solid targets produces a plasma, which flows with high velocities (of the order of 100 km/sec) into a background ambient medium. The presence of the ambient medium is very important to understand the shock formation in dilute plasma and it resembles the astrophysical plasma conditions relevant to the propagation of a supernova remnant (SNR) blast shell into the surrounding interstellar medium, both of which are at least partially ionized. The thermal expansion of warm and dense plasma into dilute plasma has been studied in experiments [4] and simulations [8], and various nonlinear structures such as ion acoustic solitons, electrostatic shocks [4] and electron phase space hole [9] have been observed as a consequence of the collision.

In this report, we present a study of the generation and spatio-temporal evolution of ECS in a tenuous plasma. The shocks are generated during the sudden expansion of laser produced plasma into a low density ambient plasma (~$3x10^{16}cm^{-3}$). ECS are seen to be propagate in the tenuous plasma and are characterized by employing a laser accelerated proton beam as a charged particle probe [11], which allows the simultaneous measurement of the spatial profile, electric field distribution and propagation velocity of the shock with a high temporal (picoseconds) and spatial (micrometers) resolution [9].

Experimental arrangement

The experiment was carried out using the VULCAN laser system in Target Area West. A laser pulse of duration 1 ns and energy 120 J was focused onto a gold foil of thickness 50µm at an incidence of 45° with the intensity ~10^{15} W/cm^2. The interaction foil was surrounded by nitrogen at pressure ~ 10^{-1} mbar. The PPI technique was employed as the main diagnostics, to detect and characterize the shock waves propagating in the low density plasma. The probing proton beam was generated from the interaction of an intense (~$5x10^{19}$ W/cm^2) laser pulse with thin gold foil; see ref [12] for experimental setup details. The proton beam, after having probed the interaction region, was recorded on a stack of several layers of Radio Chromic Films (RCF).

The ambient medium (in which the shocks propagate), is mainly ionized by the thermal radiation emitted from the laser-heated target and the parameters of the ambient tenuous plasma are estimated by simulations with the hydrodynamics Lagrangian code (HYADES) including radiation transport and ionization [14]. Hydro simulations indicate that the electron temperature and density, and ion temperature are n_e~$4x10^{16}cm^{-3}$ and K_BT_e~650eV and K_BT_i~225eV respectively, at the peak of the incident laser pulse. The Debye length of the ambient plasma is λ_{De}~1µm and the ion acoustic speed C_s~$2x10^5$m/sec. According to these parameters, the electron-electron, electron-ion, and ion-ion mean free paths are larger than the Debye length of plasma, i.e. the plasma is collisionless.

Results and Discussion

A proton image is shown in figure 1 which exemplifies the features observed in the interaction. As a rule of thumb the electric fields are directed from the regions of a lighter gray colour compared to the background (zones of reduced probe proton flux) towards the regions of darker gray colour (increased flux). A pronounced modulation in the probe proton density, revealing a strongly modulated field distribution is observed at ~1.2mm from the target. This modulation is interpreted as a shock structure propagating in the tenuous plasma at 170ps after the start of interaction. The shock has an average radius of curvature ~ 900µm, thickness δR~75µm and expands with approximately spherical symmetry from the target.

From the proton deflection pattern, one can reconstruct the

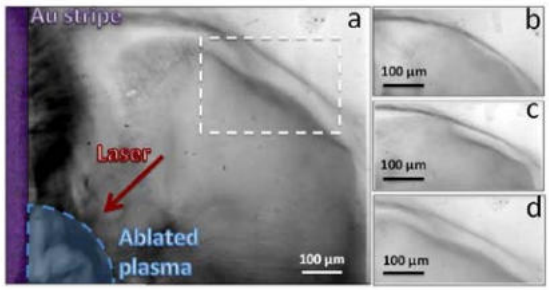

Figure 1 : (a) Proton Image of the interaction of nanosecond pulse with 50µm Au stripe, showing shock structure created during the expansion of laser-ablated plasma into tenuous plasma

electric field distribution at the shock front. The observed proton density modulation reveals that the electric field changes sign across the shock [4].

The time of flight arrangement of the proton probing provides information on the temporal evolution of the electric field distribution. Thus, the electric field profiles have been reconstructed at different probing times, and are shown in figure 2. The electric field has initially a unipolar profile and it can be interpreted as a double layer [8,14] between the front of the expanding dense plasma and the ambient plasma. The electrons from the hot plasma expand into the cold one and an electric field grows instantly at the interface. Electrons from the diluted plasma get accelerated into the dense plasma [8,15]. The double layer structure is visible in the proton image taken at 150ps (figure 2b). The reconstructed electric field and potential of this structure are shown in figures 2(a) & (c) respectively. The uni-polar electric field has amplitude of 70 MV/m and moves with velocity $2x10^6$m/sec, i.e. a Mach number ~10.

The observed modulation evolves in time into a bipolar structure, which can be taken as evidence of the onset of the formation of a shock. The reconstructed electric field shown in figure 2 (b), reveals the bipolar electric field profile. The

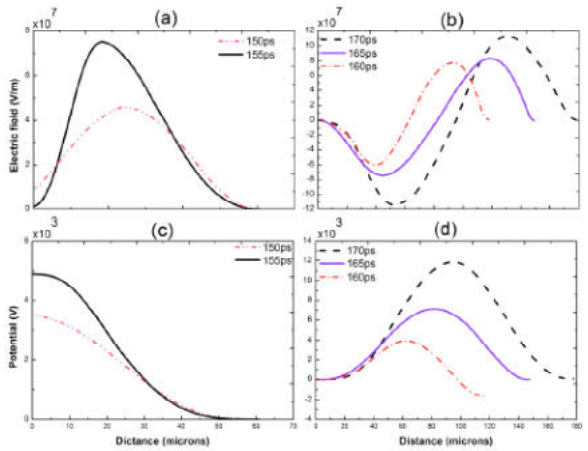

Figure 2: Experimental reconstructed electric field distribution [(a), (b)] and associated potential [(c), (d)] during the transition between the Double layer and the proto-shock. The experimental error on the electric field and position are of the order of 8% and 5 μm respectively. The profiles in (a)-(b) and (c)-(d) refer to sequential stages of the same event.

structure propagates at this stage with a velocity $8x10^5$m/sec, which is about half of the velocity of the double layer. The transition from an unipolar to a bipolar electric field occurs in a few picoseconds. Afterwards the shock structure remains stable and its propagation in the ambient plasma is observed for a further 30ps. The bipolar electric field profile can be associated with a pair of shocks (forward and reverse), each with a Mach number~4, which is close to the critical Mach number [17]. The formation of a pair of shocks by the collision of two plasmas can be described by a qualitative model, which is depicted in figure 3 (a) and described as follows. We consider two equally dense, uniform and unmagnetized plasma slabs moving in opposite directions. They consist of electrons and ions with number density n_o. The plasma slabs collide and interpenetrate, the density piles up at the overlap region close to x=0. It maintains initially its density and expands at the speed $2v_c$, where v_c is the speed modulus of both slabs as they move to x=0. Some electrons escape from the overlap layer and form a negative sheet outside of it. Therefore, the overlap layer becomes positively charged with respect to the surrounding plasma and the bipolar electric field builds up. It decelerates incoming ions and the resulting plasma compression raises the density of this layer to more than $2n_o$. If the positive potential between the overlap layer and the incoming plasma slabs is high enough to equalize the speeds of the counterstreaming ions, a downstream region forms in which the ions from both slabs can no longer be distinguished. This downstream region is confined by stable reverse and forward shocks, each of which reflects a fraction of the incoming upstream ions.

A PIC simulation has been performed to support the experimental observations, in which we study the collision of identical plasma slabs with initial parameters similar to those of the dilute plasma parameters in experiment. Each slab consists of electrons with mass m_e, number density n_o~$4x10^{16}$ cm^{-3} and Te~650eV and; singly positively charged ions with mass m_i=250m_e, having the same number density and temperature as the electrons. Each slab moves with speed v_c~$4.8x10^6$m/sec towards x=0, and collides at x=0, t=0 with relative speed of 2.75c_s, where c_s is the sound speed $c_s=(\gamma K_B T_e/m_i)^{1/2}$.

Here, we are presenting 1D simulation results only, which demonstrate the stable electrostatic shock formation with Mach no Ms=3.4. The shock speed exceeds v_c due to the expansion of the downstream region under its thermal pressure. In the early

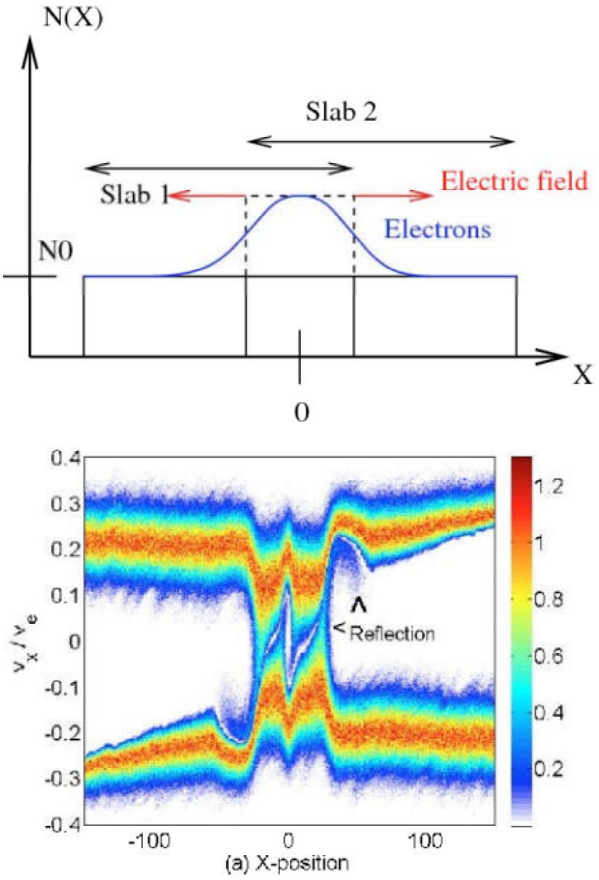

Figure 3. (top) The shock generation mechanism: Two plasma slabs with density n_0 collide at x = 0 at t = 0. The ion density close to x = 0 is ≈ 2n0 at t > 0. Some electrons escape from the ion overlap region and form an electron sheet. The charge separation gives an electric field, which accelerates ions. If the electric field is strong enough, incoming ions are reflected and a shock forms. (bottom) The ion distributions at t = 70ps, it started to mix within |x| < 20. The bulk distributions of both ion beams still interpenetrate, but fraction of incoming ions start to be reflected by the electric field.

stage of the interaction of two plasma slabs, an electric field develops instantly (<15ps after the start of interaction) between the overlap layer and the incoming plasma slabs. As the interaction between the colliding plasma slabs gets stronger, three distinct electrostatic structures appear about 50ps from the start of interaction. The ion distribution, which shows the consequence of these fields, at the time 70ps is displayed in figure 3(b). A pair of shocks has formed. The forward and reverse shocks are seen at distance x≈60 μm. These shocks confine the downstream region. Each shock is propagating into its respective upstream region, which corresponds to the part of the plasma slab that has not yet interacted with the shock. Both shocks are propagating with velocity v_s=±3.4c_s and each shock is maintained by an electric field with a peak amplitude of 0.5GV/m. This electric field matches the experimentally observed one and it is strong enough to reflect the fraction of incoming ions from both upstream region (pointed out in figure 3b), rest of the ions are still able to penetrate the positive potential of the downstream region [16].

Conclusions

In summary, we have observed the precursory stage of supercritical shock formation in laboratory plasma. The temporal evolution of electrostatic shocks in ambient plasma has been observed. In particular, we have identified in experimental data, the transition from an unipolar field profile, typical of a double layer structure, into a bipolar electric field,

and the subsequent formation of a pair of ECS. These structures is then seen to propagate in the ambient plasma with a Mach number ~4. A PIC simulation supports the existence of high Mach number (~3.4) shocks launched by collision of plasma clouds of equal electron and ion temperatures. Both experimental and simulations observed electric field are high enough to reflect fraction of the incoming upstream ions, which confirms the formation of supercritical shock.

Acknowledgements

We acknowledge support of the CLF beam access funding from STFC. We also acknowledge the support from AWE plc and the ELI project.

References

1. R.Z.Sagdeev and C.F.Kennel., Sci.Am.264, 106 (1991).

2. B. A. Remington et al., Science, 284, 1488 (1999); S.V. Bulanov et al., Eur. Phys. J.D.555, 483 (2009) ; Y. Uchiyama et al., Nature (London) 449, 576 (2007).

3. A.R. Bell et al., Phys. Rev. A. 38, 1363 (1998).

4. L. Romagnani et al., Phys. Rev. Lett. 101,025004 (2008).

5. Y. Kuramitsu et al., Phys. Rev. Lett. **106**, 175002 (2011).

6. G.Gregori et al., Nature **481**,480 (2012).

7. S.O.Dean et al., Phys. Rev. Lett. 27, 487 (1971).

8. G.Sarri et al., NJP, **13**, 073023 (2011); M.E.Diekmann et al., Plasma phys. Control Fusion 52,025001 (2010).

9. G. Sarri et al., Phys. Plasmas, 17, 010701 (2010).

10. G. Sarri et al. New Jour. Phys. 12 ,045006 (2010).

11. M. Borghesi et al., Plasma Phys. Con trol. Fusion, 43, A267 (2001); M. Borghesi et al., Plasma Phys. Control. Fusion, 50, 124040 (2008); L. Romagnani et al., laser Part.Beams, 26, 241 (2008).

12. H.Ahmed, CLF annual report, pp1-3,High energy laser interaction (2011).

13. G.Sarri et al. PRL, 107,025003 (2011).

14. S.Eliezer and A.Ludmirsky, laser Part.Beams,1, 251 (1983).

15. G. Sorasio et al., Phys. Rev. Lett. 96, 045005 (2006).

16. M.E.Dieckmann et al submitted NJP (2012).

17. D.W. Forslund and C.R. Shonk *Phys. Rev. Lett.* 25 1699 (1970); D.W. Forslund and J.P. Freidberg *Phys. Rev. Lett.* 27 1189 (1971).

18. P.Ghavamian et al APJ, 572 888 (2002).

19. T. Takeuchi et al., *Phys. Rev. Lett. 80,* 77(1998).

A comparison of different radiochromic film types

Contact *oliver.ettlinger@stfc.ac.uk*

O. Ettlinger, J.S. Green and D. Neely
Central Laser Facility, STFC
Rutherford Appleton Laboratory, Didcot, UK

D. Parker and S. Green
School of Physics and Astronomy, University of Birmingham, Birmingham, UK

Abstract

This report presents work carried out to produce absolute calibration curves for various forms of radiochromic film. It discusses the now discontinued HD-810 and presents a comparison with its replacement, HD-V2. Results show that HD-V2 is less sensitive than its predecessor, but can potentially give a greater dynamic dose range. A third, more sensitive form of radiochromic film, called EBT-2 is also characterized and discussed, including its significant potential to be used in conjunction with HD-V2 to provide 'novel' stack designs.

Preliminary work is also presented on extending the dose range for HD-V2 and EBT-2 in a similar way as discussed in a previous report by Scott et al [1].

Introduction

Radiochromic film (RCF) is a self developing, passive dosimetry film consisting of an active layer. When exposed to radiation it undergoes a polymerization reaction, increasing in optical density in proportion to deposited dose.

RCF is used in various applications, primarily in detecting electrons, X-rays and protons. Examples include those relating to medical applications; however, it is also very useful in characterizing proton beams emitted from laser-plasma interactions.

RCF allows for the typically thermal proton spectra generated during target normal sheath acceleration[2] to be characterised using a stack configuration. This incorporates layers of RCF assembled together, sometimes with a spacing material. Protons are known to deposit most of their energy at the end of their path, known as Bragg Peak energy deposition. This means that each RCF piece in the stack samples only a small number of proton energies. With this, it is possible to obtain a two-dimensional, spatial intensity profile for a proton beam at a given proton energy.

For the last few years, HD-810 has been used for detecting these laser generated proton beams. However, HD-810 was recently discontinued, and replaced with a new film, HD-V2. This report aims to discuss the similarities and differences between these two film types, along with a third film, EBT-2. The shared and contrasting characteristics of the films are explored and how they could be used to create 'novel' stack designs.

We also present results on the possibility of extending the dose range over which meaningful data can be extracted from the films.

HD-810, HD-V2 and EBT-2

As described above, RCF is a self developing dosimetry film. All three film types are similar in their design principle; however structure and composition differences provide varying dose range responses. Figure 1 shows the different film structures.

In all films, the active layer performs under the same general principle. The layer is composed of polycrystalline diacetylene, suspended in a synthetic or natural polymer[3]. When exposed to radiation, the film undergoes a polymerization reaction which forms polydiacetylene chains[4]. These exhibit a blue colour and provide the change in colour and optical density of the active layer. The number of formed chains is related to the dose deposited, and hence so is the change in optical density.

However, each of the films has a slightly different composition. In comparison to HD-810, HD-V2 has a yellow marker dye incorporated into the active layer. This provides the opportunity for the user to adjust for thickness variations in the active layer, present due to tolerances in the manufacturing process. The dye provides the ability for changes in optical density to be determined as a function of active layer thickness, and adjustments to be made. This is a feature also shared by EBT-2.

EBT-2 also has a dopant added to the active layer, a form of lithium salt[4]. This provides the film with greater low energy sensitivity, and lowers the quoted dynamic dose range of the film to 1cGy – 40Gy[3].

In contrast, HD-V2 is less sensitive than either HD-810 or EBT-2. This is supported by the quoted dynamic dose range, said to

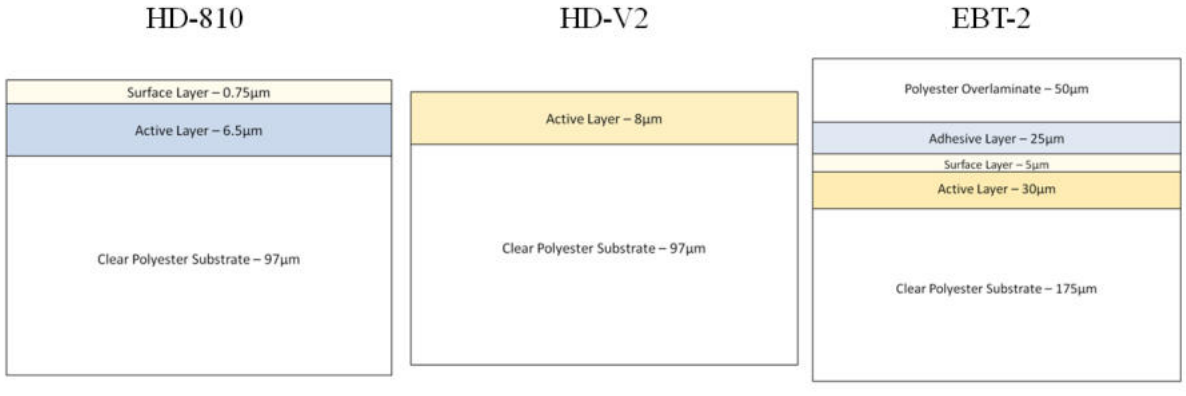

Figure 1: Schematics showing the RCF composition for HD-810, HD-V2 and EBT-2

be 10-1000Gy[5].

Film Calibration

Absolute calibration curves for the RCF are obtained by exposing the films to known doses using a cyclotron. Owing to the ability to control the proton beam current, size and energy, this allows for the dose deposited to be accurately determined and the films to be calibrated.

Once exposed to a known dose, the film is then scanned in a flatbed transmission scanner. For the purpose of this work, a Nikon Super Coolscan 9000ed[6] was used. This measures the signal from three LED sets, centred on wavelengths of 643±15nm, 532±20nm and 474±11nm through the film. 16 Bit RGB scans at 600dpi were taken, for the three film sets at different doses. The transmission of light through the films was then analysed, to determine the optical density. This was done using equation 1. It has previously been found that this should be done for each RGB channel[1] and not for the grayscale data. This helps to provide an extension to the dynamic range, due to a non-linear transmission response to optical density across the wavelength range. As a result this process was followed here.

$$OD = \log_{10}\left(\frac{\max - min}{signal - min}\right) C \qquad (1)$$

The max and min terms represent the highest and lowest possible obtainable signals when scanning no object and an opaque object (max – min therefore represents the scanners dynamic range). The signal term is the measured transmission for the film piece. The correction factor (C) is a term which converts the output into true OD and arises due to the scanner not providing absolute transmissions, but instead those as a function of the CCD response to counts levels and wavelength.

To convert from measured OD into true OD the correction factor C was obtained by scanning a series of absolutely calibrated neutral density filters and measuring the scanner response. From this, a ratio was obtained, the correction factor at a given OD. By plotting this against measured OD, one obtains a function to be used to extract the true OD.

However, the data presented here will only be with measured OD. This is still valid as calibration data for those using the scanner situated here at RAL. However, it is not compatible with any other scanner. The reason for the data not being presented as true OD is the scanner under-estimating the OD of the calibration films. The theory for this is since the LED emission is not collimated, the films experience light contamination. This 'leaks' in from the sides of the film pieces, giving artificially low optical densities. While the neutral density filters used for the calibration are relatively large and so occupy almost the whole slide; the calibration RCF films are not. Therefore while the correction factors are valid for the neutral density films, they are not for the RCF films due to the 'leaking' of light. Further work is currently underway to attempt to resolve this issue.

Results

The first features to note when observing the results are the common characteristics of the films. Figure 2 shows the red channel is optimum for low doses. This arises because it has the highest gradient and hence the greatest sensitivity.

Similarly, the blue channel is optimal for the highest doses, since it has the best sensitivity in this region. In general, switching from the red to blue channels going from low to high doses produced the most reliable data extraction regime for all films tested.

If one compares the now defunct HD-810 with its replacement HD-V2, one notices that HD-V2 is less sensitive. This can be observed across all channels by making a gradient comparison. This effectively means that one has an extension of the useable dose range of the scanner across all channels for the HD-V2 when compared to the HD-810. This is clearly visible when comparing the red channels for the two film sets.

An interesting point to note for the HD-810 is that the blue channel appears to provide a dose range up to at least 150kGy. This is nearly an order of magnitude greater than previous data[1], which found the maximum obtainable dose in the blue channel to be approx 32kGy

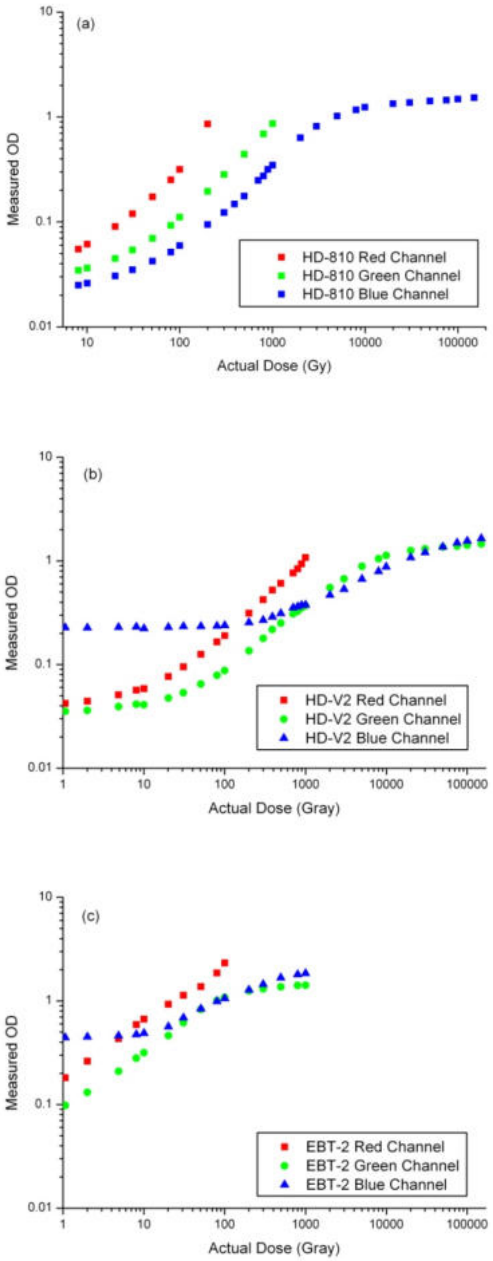

Figure 2: (a), (b), (c) Data showing the relationship between true optical density and dose for each of the RGB channels, scanning HD-810, HD-V2 and EBT-2 respectively.

In a similar vein, HD-V2 seems to be resolvable up to 150kGy in both the blue and green channels. This helps to support the notion that HD-V2 is less sensitive than HD-810.

Examining the data for EBT-2, it is clear that it is the most sensitive of all film types. This is again observed with the gradient on the channels being higher than that of other films. It also reaches higher optical densities than other films. This can be attributed to the greater sensitivity and thicker active layer

(approx. 4 times) compared with the other film types. However, with this, the film has a much lower dose range. The red channel saturates at 100Gy, whilst the green and blue channels approach saturation at ~1kGy.

The difference in characteristics between EBT-2 and HD-V2 is interesting because it provides the possibility of creating 'novel' stack designs. The thermal proton spectrum generated in a laser plasma interaction has a high flux at low energies, and a low flux at high energies. One therefore wants lower sensitivity at the front of a stack to ensure no saturation of the RCF, allowing data to be extracted. However, at the back of the stack, one needs greater sensitivity to determine the number of higher energy protons. It therefore seems logical to use a hybrid stack with HD-V2 at the front, and EBT-2 at the back, with the point of change determined by the expected proton spectra.

Dose Range Extension

It has previously been suggested that it is possible to increase the effective dynamic dose range that can be resolved[1] from HD-810 by using ultraviolet wavelengths. While it is apparent that HD-V2 is less sensitive than HD-810, ideally, we would like to be able to resolve doses up to and perhaps greater than 200kGy. The results above suggest that this will be increasingly more difficult with the flatbed scanner due to its limited dynamic range. With this, an alternative method would be required.

It is with this thought that preliminary analysis was conducted to explore whether alternative wavelengths would perhaps allow an extension to the dynamic range. This was carried out by scanning the pre-exposed films in a spectrophotometer. Wavelengths of 320nm, 1000nm and 450nm were then selected for comparison. This should allow one to see whether ultra-violet wavelengths, as suggested previously, or near the infa-red will allow for higher dose extraction.

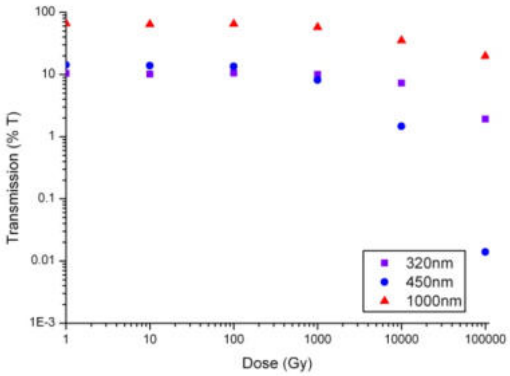

Figure 3: The transmission of ultraviolet, infa-red and blue wavelengths through HD-V2 at various, known pre-exposed doses.

Figure 3 clearly shows how the blue channel should in theory be able to reach doses approaching 100kGy, although the spectrophotometer does predict only 0.05% transmission, right at the bottom limit of its dynamic range.

Regardless of the lower transmission limit of the blue channel, the IR and UV wavelengths appear to deliver good scope for dose measurements above 1kGy, prior to which they are single-valued in their transmission and hence optical density. They both appear promising owing to the UV having greater than 1% transmission at 100kGy and the IR greater than 10%. Their gradients also indicate that they may be able to further increase their dose range, perhaps even an order of magnitude greater than the 100kGy blue channel limit. For this to be proven however, even greater doses on calibration films would be required.

The same study was also carried out for the EBT-2 film. If one could extend the dynamic dose range above its current 1kGy limit, this would make the film much more useful as a diagnostic, due to its high sensitivity and the possible higher deployable dose range. As a result, the same procedure as for HD-V2 was used and the results of this can be seen in figure 4.

Firstly, one should note that there is no UV data set owing to it having zero percent transmission at 320nm across all doses. It therefore would not be suitable for extending the dose range.

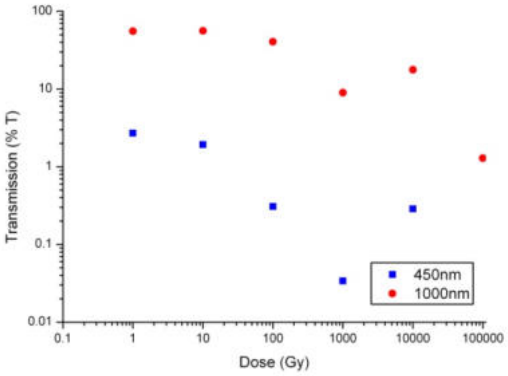

Figure 4: The transmission of blue and infa-red light through EBT-2 film, exposed to calibrated doses.

Examining the remaining two data sets, the most striking feature is the turn over which occurs in both the blue and IR regimes at 1kGy. For the blue this is a useful verification for what is seen in the data from the flatbed scanner, where again there is a limit of the channel at 1kGy.

However the IR data also shows this turnover at 1kGy. This means that it becomes multi-valued in transmission and hence no useful data can be extracted. This therefore suggests that there is no possible dose range extension through using UV or IR for the EBT-2 film.

Conclusions

RCF is a passive detection media, useful in the detection of radiation, with protons of particular interest. Three films have been examined for their relative dose responses. These were HD-810, HD-V2 and EBT-2. It was found that EBT-2 is the most sensitive of the three, although the effective dose range quoted by the manufacturer can be extended by over an order of magnitude.

After analysis, it was also discovered that the now discontinued HD-810 film was more sensitive than its replacement, HD-V2. This is of interest, because it provides the opportunity to extract higher dose measurements from the new film, when HD-810 would have become saturated. This helps one to argue that HD-V2 is a more than adequate replacement for HD-810, given doses at the front of the RCF stack are known to exceed 200kGy, a dose that is not readable with standard flatbed scanning techniques in the visible range.

With this, preliminary work was shown on extending the dynamic dose range of HD-V2 and EBT-2 using ultraviolet and infa-red wavelengths. It was found that EBT-2 could not be extended, due to the characteristic turn-over of the transmission in the 1kGy region. However, this data obtained using the spectrophotometer agreed with that from the flatbed scanner for the blue channel. In contrast, HD-V2 was found not to have this turnover at doses up to 100kGy, and along with the transmission levels for the IR and UV wavelengths, it can be seen that a dose range extension is plausible. Work is now underway to design and implement a CCD-based film scanner that can be used with either an IR or UV backighter.

References

1. G. Scott *et al.* CLF Annual Report 2010-2011
2. Hatchett S P *et al.* Electron, photon, and ion beams from the relativistic interaction of petawatt laser pulses with solid targets *Phys. Plasmas* **7** 2076–82 (2000)
3. EBT-2 manufacturer product specification sheet http://online1.ispcorp.com/_layouts/Gafchromic/content/products/ebt2/pdfs/EBT2productSpec.pdf
4. D. Kirby *et al.* LET dependence of GafChromic films and an ion chamber in low-energy proton dosimetry *phys. Med. Biol.* **55** 417-433 (2010)
5. HD-V2 manufacturer product specification sheet http://online1.ispcorp.com/en-US/gafchromic/Pages/ProductDetail.aspx?BU=GafChromic&prdId=40930
6. http://www.nikonusa.com/Nikon-Products/Product-Archive/Film-Scanners/9237/Super-COOLSCAN-9000-ED.html

The Effect of Lattice Structure on Fast Electron Transport in Warm Dense Carbon

Contact *david.maclellan@strath.ac.uk*

D. A. MacLellan, D .C. Carroll, R. J. Gray, H. Powell, G. G. Scott*, P. McKenna

SUPA, Department of Physics, University of Strathclyde, Glasgow G4 0NG, UK

A. P. L. Robinson, N. Booth, D. Neely

**Central Laser Facility, STFC Rutherford Appleton Laboratory, Oxfordshire OX11 0QX, UK*

M. P. Desjarlais

Sandia National Laboratories, P.O. Box 5800, Albuquerque, New Mexico 87185, USA

M. Burza, C.-G. Wahlström

Department of Physics, Lund University, P.O. Box 118, S-22100 Lund, Sweden

X. H. Yuan, D. Fei

Beijing National Laboratory of Condensed Matter Physics, Institute of Physics, CAS, Beijing 100190, China

Introduction

In recent years the ability to use intense laser-solid interactions to create extreme states of matter that have previously only existed in astrophysical scenarios has attracted considerable interest. One example is the state of matter known as 'warm dense matter' (WDM), which exists at densities of 0.1-10 g/cc and temperatures of 1-100eV[1]. Developing our understanding of WDM is not only important at a fundamental physics level, but also in applications such as Inertial Confinement Fusion [2]. Understanding the transport properties of large currents of energetic electrons (MeV) in WDM is particularly important for the fast ignition approach to inertial confinement fusion [3], the development of laser-driven ion sources [4], and for laboratory astrophysics.

During the interaction of an intense laser pulse with a solid target, a significant fraction of the laser energy is absorbed, producing a multi-mega-Ampere current of relativistic electrons. The transport of this current within the solid is subject to transverse and longitudinal instabilities, which can result in filamentation of the beam during propagation. There are a number of plasma instabilities that can result in filamentation, including the Weibel [5, 6], two-stream [7], and resistive filamentation instabilities [8].

It is well known from solid state physics that the electrical conductivity of a material is strongly affected by its lattice structure [9]. The mega-Ampere currents of electrons produced in an intense laser-plasma interaction greatly exceed the Alfven limit [10], and thus to enable the fast electrons to propagate a return current of thermal electrons, drawn from the background material, must propagate in the opposite direction. This return current is highly collisional, and rapidly heats the target. The material undergoes a transition from cold solid, via a transient state of WDM, to hot plasma. The duration of the fast electron bunch, which drives the target heating by drawing the collisional return current, is of the order of the laser pulse duration. In the case of a short, 1ps pulse, the fastest electrons at the leading edge start heating the target and the remaining electrons propagate through the resulting transient state of WDM on a picoseconds timescale. The background electrons are rapidly heated in femtoseconds, but the energy transfer to ions typically takes tens of picoseconds. As a result, the picosecond electron bunch passes through a transient state of WDM in which the electrons are hot but the ions temporarily remain cold and retain the structural arrangement they possessed in the condensed matter state [11]. The electrical conductivity of the material in this transient state is thus affected by the lattice structure of the ions.

In this report, we present preliminary results from an investigation of the effect of lattice structure on fast electron transport. Using various forms (allotropes) of the same element, carbon, we show that lattice structure can determine whether or not fast electron beam filamentation occurs in solid targets irradiated by intense picosecond laser pulses. By investigating this at two laser intensities, 4×10^{19} Wcm^{-2} and 3×10^{20} Wcm^{-2}, we also show that the onset of electron beam filamentation is sensitive to the drive laser pulse energy.

Experiment

The experiment was performed in two parts. The first part was performed using the Vulcan laser in Target Area Petawatt (TAP), delivering pulses of 1.053 µm wavelength light, with energy on target of 200 J and duration equal to 1ps at FWHM. The p-polarized pulses were focused to a 7 µm diameter FWHM spot, with a calculated peak intensity of 3×10^{20} Wcm^{-2}. The second part was performed using the Vulcan laser in Target Area West (TAW). In this arrangement, the laser delivers 1ps, 1.053 µm pulses with an on target energy of 60 J. Again, the p-polarized pulses were focused to a focal spot of 7 µm diameter at FWHM. The resulting peak intensity is calculated to be 4×10^{19} Wcm^{-2}. The main target samples were two different allotropes of carbon: (1) single-crystalline diamond (highly ordered lattice) and (2) vitreous carbon (highly disordered carbon). Whereas single-crystalline diamond contains a highly ordered face-centred-cubic lattice structure, vitreous carbon exhibits a highly disordered, asymmetrical structure.

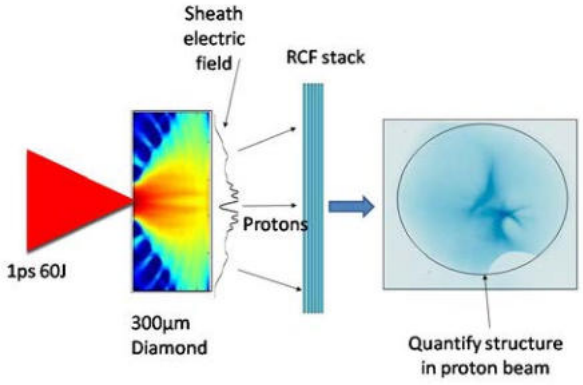

Figure 1: Simplified schematic of the experimental setup used to measure the fast electron beam instabilities.

The fast electron transport pattern inside the target is diagnosed by recording and analyzing the spatial-intensity profile of the proton beams accelerated from the target rear surface. The

accelerated protons are a result of an electrostatic sheath field established by the fast electrons at the target rear surface [12]. Fuchs *et al*. [13] have previously demonstrated that modulations in the sheath field, as a result of filamentation of the electron beam within the target, are directly mapped into the expanding proton beam spatial-intensity distribution [14]. We have developed an analytical model to determine how the structure within the electron density at the rear side of the target is mapped into the expanding beam. This is described by Quinn *et al* [14]. A stack of radiochromic dosimetry film, which enables measurement of the dose deposited by the proton beam at discrete energies given by the stopping range of protons within the stack, is used to measure the spatial-intensity distribution of the proton beam. Each piece of film was optically scanned and the modulations within the proton dose quantified using image analysis algorithms.

Experimental Results

Figure 2 shows the experimentally measured proton beam spatial intensity profiles for the two mean carbon allotropes, as well as comparing the results for diamond at two discrete laser intensities. A smooth spatial-intensity profile is measured for the diamond target at $3x10^{20}$ Wcm^{-2}, shown in Figure 2(a), whereas the proton beam profile is highly structured in the case of vitreous carbon. These results are discussed in more detail in McKenna *et al* [15]. The fact that diamond, one of the best electrical insulators at room temperature, exhibits smooth electron transport was initially surprising, because stronger filamentation is typically measured with insulator targets, compared to metals. At the lower intensity of $4x10^{19}$ Wcm^{-2}, the spatial intensity distribution of the proton beam in the same diamond target begins to exhibit a signature of the onset of fast electron beam filamentation. Specifically, modulations are measured in the centre of the proton beam only. Figure 2(d) shows the variation in the proton beam dose as a function of radius, averaged over a number of sample angles.

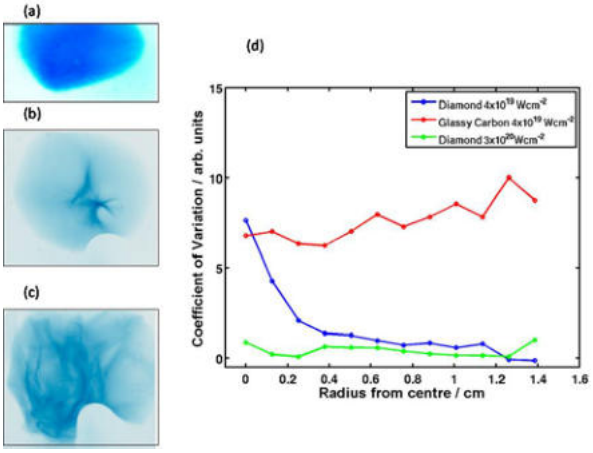

Figure 2: Spatial-intensity profile measurements of the proton beam, at energies of 10 MeV for (a) diamond at $3x10^{20}$ Wcm^{-2} and 5.6 MeV for (b) diamond at $4x10^{19}$ Wcm^{-2} and (c) vitreous carbon at $4x10^{19}$ Wcm^{-2}. (d) Radial variance analysis of the proton signal for each target material, in which the variation in the proton beam dose as a function of radius is calculated.

Although not shown, reference shots were taken with pyrolytic carbon which displayed an intermediate degree of beam filamentation, corresponding to an intermediate degree of ionic ordering. Repeat shots were taken on each of the allotropes and intensities and the results are fully reproducible. These results are explained by the effect of lattice structure on electrical conductivity and the fact that the lattice structure is temporarily maintained during rapid thermal excitation of the material, as discussed above [15].

Modelling

To investigate this in more detail, the electronic structure and electrical conductivity of the two different allotropes of carbon were modelled: diamond (tetrahedral lattice) and vitreous carbon (disordered) as a function of temperature. The electrical conductivities were derived using quantum molecular dynamics (QMD) calculations with VASP, a plane-wave density functional code, the details of which are given in other publications [16, 17]. The results of these QMD calculations are shown in Figure 3.

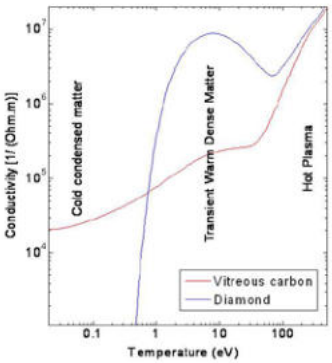

Figure 3: Calculated electrical conductivity as a function of temperature for diamond and vitreous carbon.

The physical origin of the effect of ionic ordering on electrical conductivity in this transient WDM is based on the electron mean free path in the material [9]. If the ions are highly disordered, then electrons scatter incoherently and the electron mean free path is limited to the mean inter-ionic distance. By contrast, if the ions are in a well-ordered geometric lattice, the electrons scatter coherently, leading to constructive interference of the scattering of the wave function from multiple ions, resulting in a mean free path considerably longer than the mean inter-ionic distance. Thus, for an ordered ionic structure the material conductivity is larger than for a disordered material of the same atomic element. As the temperature increases beyond 100 eV, the scattering cross sections diminish and ionisation dominates, hence the conductivity increases irrespective of ionic ordering.

To understand how these differences in conductivity affect the fast electron transport, a program of simulations is underway using the 3D ZEPHYROS particle-based hybrid code [18], using these calculated conductivity curves as an input parameter.

The observed differences in the fast electron transport patterns upon varying the laser energy is investigated. Since the magnitude of the collisional return current is proportional to the current of the fast electron beam, which in turn is proportional to the laser energy, the temperature of the transient WDM achieved during transport of the fast electrons is likely to be significantly lower in the case of the lower laser intensity shots. Further analysis and simulations are presently underway to investigate this further.

Conclusions

In summary, these results show that in the interaction of a short high intensity laser pulse with a solid target the lattice structure affects the fast electron transport properties. The electrical conductivity of the resulting transient state of WDM on

picoseconds timescales is determined by the lattice structure because on this short timescale the background electrons are hot, but the ions are cold. These findings show that choice of allotrope of a given material is important in fast electron transport, which may influence the choice of materials used for example in advanced schemes for inertial confinement fusion [4].

Acknowledgements

We acknowledge the expert support of the staff at the Central Laser Facility of the Rutherford Appleton Laboratory and the use of computing resources provided by the STFC e-Science Facility. This work is supported by EPSRC (Grants No. EP/E048668/1 and No. EP/E035728/1), the HiPER project, the Swedish Research Council, and by the National Basic Research Program of China (program 973; Grant No. 2007CB815101).

References

[1] R. W. Lee *et al.,* J. Opt. Soc. Am. B 20**,** 1 (2003).

[2] Nuckolls *et al.,* Nature, vol 239, 139 (1972).

[3] M. Tabak *et al*., Phys. Plasmas 1, 1626 (1994).

[4] M. Borghesi *et al*., Fusion Sci. Technol. 49, 412 (2006).

[5] E. S. Weibel, Phys. Rev. Lett. 2, 83 (1959).

[6] Y. Sentoku *et al*., Phys. Rev. Lett. 90, 155001 (2003).

[7] B. Hao *et al*., Phys. Rev. E 79, 046409 (2009).

[8] L. Gremillet, G. Bonnaud, and F. Amiranoff, Phys. Plasmas 9, 941 (2002).

[9] J. M. Ziman, Adv. Phys. 16, 551 (1967).

[10] H. Alfven, Physical Review, vol. 55, 425 (1939).

[11] S. Mazevet *et al.,* Phys. Rev. Lett. 95, 085002 (2005).

[12] S. C. Wilks *et al.,* Phys. Plasma, 8, 542 (2001).

[13] J. Fuchs *et al*., Phys. Rev. Lett. 91, 255002 (2003).

[14] M. N. Quinn *et al.,* PPCF, 53, 124012(2011)

[15] P. McKenna *et al.*, Phys. Rev. Lett, 106, 185004 (2011).

[16] G. Kresse and J. Hafner, Phys. Rev. B 47, 558 (1993).

[17] M. P. Desjarlais, J. D. Kress, and L. A. Collins, Phys. Rev. E 66, 025401 (2002).

[18] S. Kar *et al.*, Phys. Rev. Lett. 102, 055001 (2009).

X-ray scattering from liquid carbon heated by laser-accelerated protons

Contact *A.Otten@gsi.de*

A. Otten, K. Siegenthaler, D. Kraus, M. Roth

Technische Universität Darmstadt
Schlossgartenstr. 9, 64291 Darmstadt, Germany

T. White, C. Murphy, G. Gregori

Oxford University
Parks Road, Oxford, OX1 3PU

T. Dzelzainis, B. Kettle, S. White, D. Riley

Queen's University Belfast
University Road, Belfast BT7 1NN

M. Notley

Central Laser Facility
Rutherford Appleton Laboratory, Didcot, OX11 0WX, U.K.

Introduction

Although carbon is one of the most common elements on earth, knowledge about its thermodynamic behaviour at high pressure and temperature is limited. Equation of state data stem almost entirely from modeling and show a wide variation depending on the different theoretical approaches. The phase boundaries, including the melt line, are still poorly understood. In fact, at ambient pressure carbon does not melt but sublimes into the gas phase. As it is difficult to achieve the required extreme conditions of high presssure and temperature, little experimental data is available.

However, liquid carbon may exist at the core of giant planets like Uranus and Neptune, in white dwarfs or carbon-rich extrasolar planets [1, 2]. Accurate equation of state data are needed to develop realistic models of planetary formation or the structure of giant planets. The melt line of carbon can have far-reaching implications on the assumed liquid content and thus the modeling of the magnetic fields of planets [3]. Furthermore, carbon melt data can serve as a test for warm dense matter theories.

In this report, we present first results from an experiment conducted at VULCAN, where carbon samples were heated and molten by laser-accelerated proton beams. The phase transition was observed with x-ray scattering.

Generating liquid carbon

Our approach to generate liquid carbon is to heat a carbon sample isochorically and instantaneously with laser-accelerated protons. Unlike laser beams which only interact with the surface, protons deposit their energy in the whole sample. The energy spectrum of laser-accelerated protons is exponential. While this broad spectral range is a disadvantage to some applications, it is ideal for the task of heating a thick carbon sample. A wide energy spread means that at each depth in the sample a large number of protons with the appropriate Bragg peak deposits their energy. The proton energies required to heat a 150 µm thick carbon sample range between 1 and 5 MeV.

The VULCAN beam 8 was focused on a thin aluminium foil to generate a proton bunch which then heated a 150 µm thick carbon sample at 1 mm distance. The laser pulse duration was 11 ps, the energy was 150 J before the compressor. Compared to many laser-ion acceleration experiments, the laser intensity was kept relatively low without reducing the beam energy. The resulting proton energy spectra therefore had a low cut-off below 10 MeV with large proton numbers of more than 10^{13}. As the carbon sample is heated most efficiently by the low-energy protons, those spectra were well suited for heating the sample.

With these proton beam parameters, the carbon samples were heated to temperatures of a few thousand Kelvin at pressures of several GPa and solid state density. As melting takes place at ca 4500 K, the samples were partly molten.

X-ray scattering from the sample

The power of radiation scattered into the solid angle $d\Omega$ by the electrons in a sample is described by the following equation [4]:

$$P_S\, d\omega\, d\Omega \;=\; \frac{P_0 r_0^2 d\Omega}{2\pi A} N S(\boldsymbol{k},\omega) d\omega \frac{1}{2}(1+\cos^2\theta)$$

Here, $\boldsymbol{k}$ is the momentum transfer to the electrons and ω is the frequency shift of the photons. For small momentum transfers, $\boldsymbol{k}$ only depends on the scattering angle and the wavelength of the radiation, i.e. it is completely defined by the experiment geometry. N is the number of scattering electrons in the sample, A the irradiated area and r_0 the classical electron radius. All the material's properties are expressed in the dynamic structure factor $S(\boldsymbol{k},\omega)$ which is the Fourier transform of the density modulations in the sample. It contains contributions from the free, bound and weakly bound electrons which undergo a bound-free transition during scattering. For the expected temperature range, ionisation of the sample is negligible and there are no free electrons. The static structure factor $S(\boldsymbol{k}) = \int S(\boldsymbol{k},\omega) d\omega$ can then be written as a sum of two contributions from the tightly bound electrons and inelastic scattering from weakly bound electrons [5, 6]:

$$S(\boldsymbol{k}) \;=\; |f(\boldsymbol{k})|^2 S_{ii}(\boldsymbol{k}) + Z_{wb}\left(1-\left(\frac{f(\boldsymbol{k})}{Z}\right)^2\right)$$

$f(\boldsymbol{k})$ is the atomic form factor. While the bound-free contribution is equal for solid and liquid carbon, the ion-ion structure factor $S_{ii}(\boldsymbol{k})$ changes significantly. It is the fourier transform of the pair correlation function and therefore reflects the microscopic structure of the sample. At the chosen $\boldsymbol{k}$ vector graphite does not have a Bragg peak, which is expressed in a small S_{ii} value. On the other hand, S_{ii} at the given **k** vector reaches its maximum when the sample is just above the melting temperature [3]. A phase transition is therefore imprinted in the total scattered signal.

Experimental setup

The experiment was carried out in the target area west of the VULCAN laser system. The target is shown in figure 1. The short pulse beam 8 was focused on a 20 µm thin aluminium foil and accelerated a proton bunch from the rear side. The laser pulse had a duration of 11 ps and an energy of 150 J before the compressor. The protons penetrated a 150 µm thick carbon foil at 1 mm distance from the aluminium foil and heated it isochorically. To shield the spectrometer from the intense x-ray radiation produced in the short pulse laser-matter interaction, the aluminium foil was placed inside a hollow gold cone. The sample was probed by He-α radiation from a plasma generated by four long pulses irradiating a 10 µm thick titanium foil. Each longpulse had a duration of 1 ns and an energy of 100 J at 527 nm. The x-rays were incident on the carbon rear side at an angle of 45° and were scattered to the spectrometer with a scattering angle of 90°. To shield the direct line of sight to the spectrometer, the titanium foil was also placed in a cone.

Those protons that travelled through the carbon foil were stopped in a stack of radiochromic films (RCF). From comparison with reference shots on a freestanding aluminium foil, the proton spectrum and thus the energy deposited in the carbon sample were determined from the RCFs for each shot.

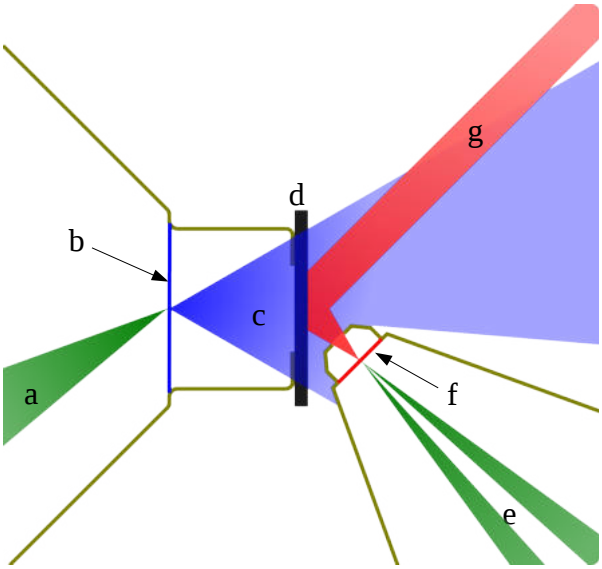

Figure 1: Target. a) CPA beam 8, b) aluminium foil, c) laser-accelerated protons, d) carbon foil, e) long pulse beams, f) titanium foil, g) scattered x-ray radiation

The scattered radiation was detected by a highly efficient HOPG spectrometer in von Hamos geometry. Another HOPG spectrometer directly monitored the intensity of the x-ray source radiation.

Experimental results and their analysis

Figure 2 shows an example of a stack of radiochromic films. Protons with different energies are stopped in different films, so each film represents a different part of the proton spectrum. Only a part of the beam arrived at the RCF stack, the rest was stopped in the x-ray cone target. The detected fraction of the full beam was derived from comaprison with reference shots, i.e. shots without x-ray target. The dose on each film is mainly due to the protons which have their Bragg peak in the RCF, but also higher energetic protons which pass through the film contribute to the dose. Using a proton-energy dependent dose calibration of the RCF [8], an exponential energy distribution was fitted to the measured doses, taking into account the detected fractions.

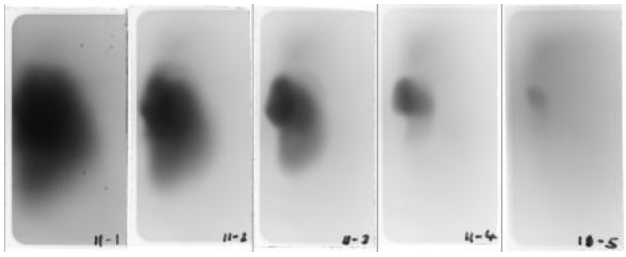

Figure 2: A part of the accelerated protons is recorded with a radiochromic film stack.

The energy distribution has the form

$$\frac{dN}{dE} = \frac{N_0}{E}\cdot\exp\left(-\frac{E}{k_B T}\right)$$

with $N_0 = 1.0 \cdot 10^{14}$ and $k_BT = 1.09$ MeV. The result of the fit for the RCFs in figure 2 is shown in figure 3. The cutoff energy of 9 MeV is rather low, while the total proton number is more than $2 \cdot 10^{13}$.

The energy deposition in the sample was calculated using the SRIM code [9]. Assuming the SESAME [10] equation of state for graphite and the density of the solid sample, the temperature profile in figure 4 is obtained. A horizontal line marks the

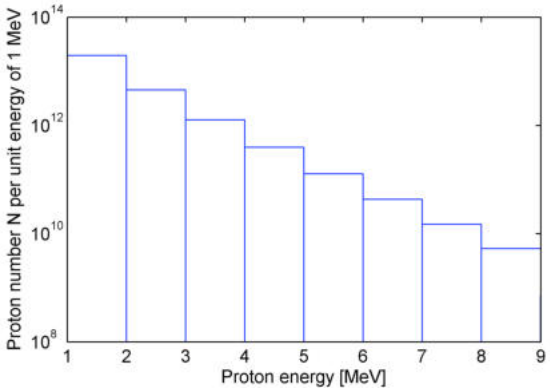

Figure 3: Proton numbers per 1MeV energy interval

approximate melting temperature of 4500 K. About half of the sample is therefore molten.

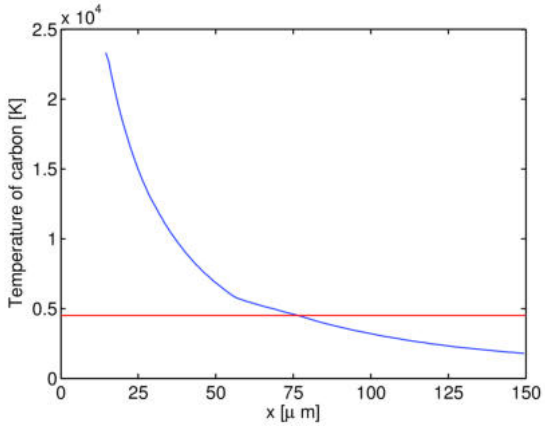

Figure 4: Calculated temperature profile using SESAME equation of state. The horizontal line is at 4500 K, the approximate melting temperature. The protons penetrate the sample from the left side.

The melting is clearly visible in the x-ray scattering data (figure 5). The scattered spectrum from heated graphite is plotted together with the scattered spectrum from unheated samples. The scattered spectra have been scaled to take into account different source strengths on dirfferent laser shots. Their intensity differences are therefore only due to different microscopic structures. Due to the higher structure factor of liquid carbon the scattering signal from heated graphite is

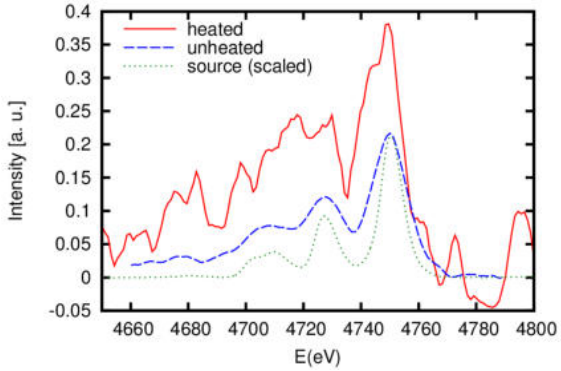

Figure 5: Measured x-ray spectra. The source spectrum is scaled to size to illustrate the spectral form of the source.

significantly increased. For a further analysis and a comparison with equation of state models, the target geometry has to be considered. Firstly scattering from different depths in the sample is affected by x-ray attenuation, secondly other scattering angles than 90° also contribute to the scattering signal.

Conclusions

Using laser-accelerated protons, carbon samples were heated to temperatures near the melting point at ca 4500 K. The microscopic structure of the heated samples were investigated by scattering He-α x-ray radiation from a laser-generated Ti plasma. The phase transition causes an increase in the total scattered intensity compared to unheated samples.

Acknowledgements

We would like to acknowledge the support from the VULCAN laser team, from the target area staff and from the target fabrication. The work of A. O., D. K. and M. R. was supported by the BMBF, support code 06DA9043I.

References

1. P. Dufour *et al*, Nature **450**, 522 (2007).
2. W. B. Hubbard *et al*, Science **253**, 648 (1991).
3. S. Stanley & J. Bloxham, Nature **428**, 151 (2004).
4. S. H. Glenzer & R. Redmer, Rev. Mod. Phys. **81**, 1625-1663 (2009)
5. R. James, *The optical principles of the diffraction of x-rays*, G. Bell, London, (1962)
6. G. Gregori *et al*, Electronic structure measurements of dense plasmas, Physics of Plasmas **11**, 2754-2762 (2004)
7. J.-P Hansen. & L. Verlet, Phys. Rev. **184**, 151-161 (1969)
8. F. Nürnberg et al, Review of Scientific Instruments **80**, 033301 (2009)
9. J. F. Ziegler *et al*, *SRIM. The Stopping and Range of Ions in Matter*, SRIM Co. (2008)
10. J. Johnson & S. Lyon, SESAME 07832 (1993)

Modelling channel formation by high intensity laser plasmas

a.rehman07@imperial.ac.uk

A. Rehman, Z. Najmudin, A.E. Dangor
Blackett Laboratory, Imperial College London, SW7 2BZ

P.A. Norreys
STFC Rutherford Appleton Laboratory, Chilton, OX11 0QX

Abstract

This report represents results from 2D PIC simulations with the code OSIRIS showing plasma channels created by focusing either a 1ps or 30 ps pulse with peak intensity of 3×10^{18} Wcm^{-2} into a hydrogen gas.

This channel is produced (primarily) from the radial expulsion of plasma due to the ponderomotive force of the laser. The size of the plasma channel was measured to be mm in scale and the dynamics of the process involve laser self-focusing and filamentation of the plasma channel for higher densities. A good match is found in most cases between the simulations and previously reported experimental observations, though small deviations occur at higher densities.

Introduction

The propagation of an intense laser pulse through fully ionised plasma has been investigated extensively in the last decade (1). There are a number of applications that require the formation of a stable channel in underdense plasma. These include laser wakefield acceleration of electrons (2), high brightness x-ray generation by betatron emission (3) and the fast ignition variant of inertial confinement fusion (4).

In particular, fast-ignition has intensified the interest in studying the generation of hot electrons produced by laser-matter interaction. There are several mechanisms, by which an ignition laser pulse in fast ignition (FI) can reach close to the core. In the case of hole-boring, the ignition pulse needs to make a hole through an underdense plasma to reach near to critical surface with a critical density $n_{cr} = \omega_p^2 \sum_0 m_e/e^2$ (4). A short intense laser injected close to the precompressed dense core at maximum compression, can deposits it energy efficiently into suprathermal electrons at the critical density surface. These suprathermal electrons propagate from the critical density to the high-density core and initiate fusion. As the Vulcan Petawatt, is capable of delivering peak powers of hundreds of terawatts, it is interesting to examine the acceleration of hot electrons occurring at these high intensities which are comparable to those required for fast ignition (6). It is of course also interesting to see how such intense pulses tunnel through the underdense plasma regions prior to the core.

Tabak et al. (6) also proposed adding a longer intense pulse (duration ~100 ps) ahead of an ignition pulse in order to generate a channel in the underdense corona surrounding a fusion pellet in order to push the critical surface of the plasma closer to the dense core. This scheme has several advantages as compared to adding an external guide as in the cone-guided concept (6). It requires less sensitive target fabrication, and may therefore be easier to implement. It also decreases the cost of targets and may lead to more efficient coupling of laser energy to the core for fast ignition.

Relativistic channelling in underdense plasma has been studied both computationally (7) and experimentally (8). Different plasma densities, laser powers and pulse shapes have been considered for the process of plasma creation and channelling. In the high intensity regime ($a_0 \geq 1$), the ponderomotive force (9) and relativistic effects (10) dominate the laser plasma interaction. Theses forces can modify the refractive index of the plasma leading to self-focusing and filamentation. These studies also show that high intensity laser plasma interactions also leads to other detrimental instabilities, such as longitudinal modulation, induced by self-focusing (11), and long wavelength hosing (12). An experiment to investigate these issues was conducted at the Rutherford Appleton Laboratory. The aim of the experiment was to study laser channelling in underdense plasma by laser pulses of comparatively long duration, emulating the one proposed by Li et al. (1), focused into a supersonic gas jet at various densities. It was shown that even when the laser power is below the threshold for relativistic self-focusing the ponderomotive force is able to create a longitudinally smooth channel (10).

Formation of plasma channel with short pulse laser

For the experiment being simulated (13), Vulcan Petawatt delivered pulses of up to 155 − 250 J on target with pulse duration $\tau_L = 740 \pm 130$fs. An *f*/3 off-axis parabolic mirror was used to focus these pulses onto the edge of a supersonic gas jet, producing intensities $\gtrsim 10^{21}$ Wcm^{-2}, which corresponds to a normalised vector potential of $a_0 = eE/m_e > 20$.

For a better understanding of the physics involved in this experiment, a series of relativistic 2D3V PIC simulations were

performed with the code OSIRIS. Simulations are usually performed in normalised units. In theoretical plasma physics, division of quantities by several constants (m_e, e, and c) to leave dimensionless quantities is common. To initialise the simulations, the input parameters of the density profile and the chosen laser parameters were prepared using the normalised units shown in table 1.. The output data of the simulation are also in these normalised units.

Parameters	Osiris Unit
Length	c/ω_0
Time	$1/\omega_0$
Velocity	c
Charge	e
Mass	m_e
Momentum	$m_e c$
Density	$n_c = \sum_0 m_e \omega_0^2 / e^2$
Electric field	$m_e c \omega_0 / e$

Table 1 The normalised units used for the OSIRIS simulation

The simulations investigate the laser propagation and electron acceleration at different plasma densities. In our simulation, the laser pulse was modelled with a peak normalised vector potential $\sim a_0 = 15.6$ and pulse duration $\tau_{FWHM} = 660$ fs. The slightly lower initial a_0 was designed to not overestimate the influence of laser energy once the laser diffracts, which is a problem for 2D simulations. Within the simulations the spatial profile is a perfect gaussian, with 50% of the total laser energy within the FWHM. This was not the case during experiment, where the wings of the beam contain more energy, and also motivates using lower initial a_0.

The simulation box for these simulations was stationary. A 660 fs long pulse with a gaussian temporal shape was focused to the edge of a fully ionised hydrogen plasma. The simulations were carried out, with varying plasma electron density $n_e = (0.001 n_{cr} - 0.1 n_{cr})$. The laser propagated in the box from the left boundary to the right boundary. The simulation box was approximately 25 mm with a resolution of 12.56 cells/λ_0 in the transverse (y) direction and 1.58 mm cells/λ_0 in the longitudinal direction (x). Simulation data was saved after a time step corresponding to every 0.49 ps. Importantly the colour tables are rescaled based on the peak values in each case. This allows greater detail to be visible.

Simulations Results

Figure 1 shows snapshots of the transverse electric field (i.e. the laser) on the left and the electron number density of the plasma on the right for density $n_e = 1 \times 10^{18}$ cm^{-3} for $\sim$2.4 ps, 4.9 ps and 7.3 ps. The formation of a plasma channel can be easily ascribed to the effects of ponderomotive forces associated with the intense laser pulse as it propagates through the plasma. Initially, the laser pulse exerts a ponderomotive force on the electrons and expels them radially. This sets up a large space charge force that pushes the ions outward from the axis of propagation. After the passage of the laser pulse, the ions continue to drift radially approximately with velocity associated with the ponderomotive potential U_{pond}, and thus creating a plasma channel. This leads to a shock-like structure is set up which expands away from the laser axis. Longitudinal electric field plots show that the longitudinal fields are negligible as compared to the transverse fields due to the cavitation. This means wakefields are suppressed and so all the acceleration must be due to direct laser acceleration (14).

Figure 2 shows the corresponding density profiles at times 3.9 ps and 5.8 ps into the simulation for an initial plasma density $n_e = 1{\times}10^{20}$ cm^{-3}. In this case, the beam propagation has become severely filamented and laser propagation is strongly inhibited due to energy conversion into hot electrons.

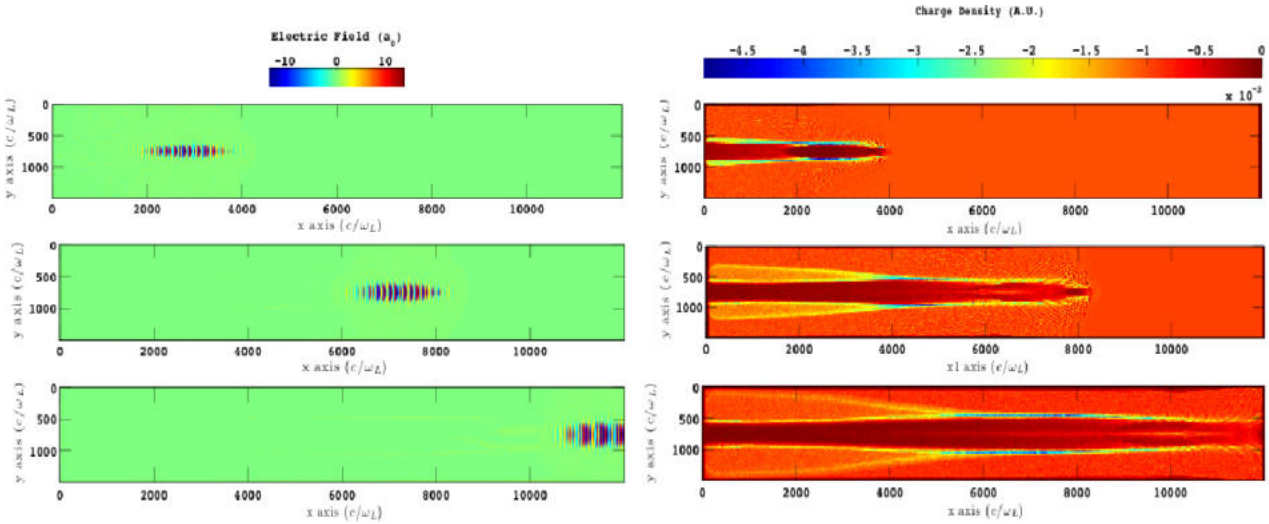

Figure 1: Osiris PIC code simulation results at $n_e = 0.001 n_{cr} = 1 \times 10^{18}$ cm^{-3}. From left to right, transverse (laser) electric field and electron number density. These are all shown for the same time step in the simulation from top to bottom, 2.4 ps, 4.9 ps and 7.3 ps.

Figure 3 shows electron spectra obtained at time 1.9 ps into interaction for different densities, from $0.001n_{cr}$ - $0.1n_{cr}$. An exponentially decreasing electron spectrum is produced (broad energy spread) produced in each case with temperature.

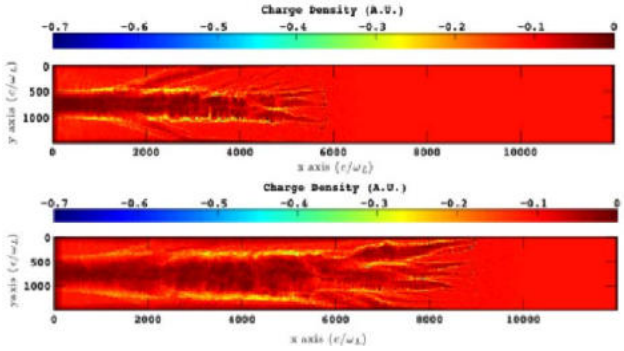

Figure 2: 2D3V Osiris PIC code results showing the electron number density at 3.9 ps and 5.8 ps for an initial density is n_e=0.1n_{cr}.

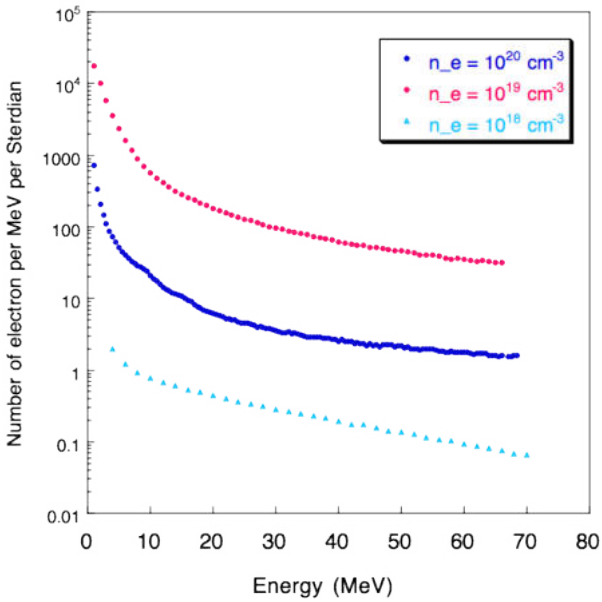

Figure 3: Variation of electron energy spectra with initial electron number density

It can be summarised, that such interactions can produce relativistic bunches of electrons with energies up to 100 MeV, and particularly at high density lead to filamented laser propagation. The observed maximum energy of these electrons reaches to beyond 60 MeV for all of the simulations., with a distribution function that is quite similar in all three cases, though perhaps with a more pronounced two temperature bend in the curve for higher densities. However the numbers of electrons accelerated decreases rapidly with decreasing plasma density, by ≈100 times from $0.1n_{cr}$ to $0.01n_{cr}$, and by an even greater margin from $0.01n_{cr}$ to $0.001n_{cr}$. Hence though it may be that the highest energy electrons may be produced at the lowest densities, the efficiency of conversion into hot electrons reduces rapidly. Indeed the numbers of electrons at the lowest density are so few that they would be difficult to detect and indeed in the experiments, no such hot electrons were detected at $0.001n_{cr}$. The increase in electron energies (temperature) increase for decreasing density is shown explicitly in figure 4, which shows the same dependence as seen in the experiment (at densities where electrons were observed) with mean energy at 10^{19} cm^{-3} at T_{eff} < 15 MeV as opposed to the experimentally determined value of T_{eff} < 18 MeV.

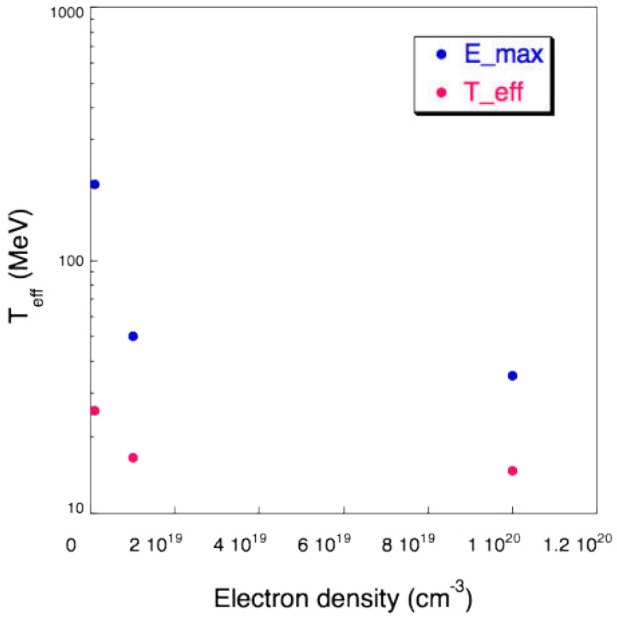

Figure 4: Variation of temperature with the given electron number density

Such energetic electron production would be a problem in ICF, since these electrons would have a much larger range than would be ideal for fast ignition. Furthermore, as in real hole-boring experiment the ignition laser pulse duration is proposed to be much longer [7], which will have major implications as is discussed in the next section.

Formation of plasma channel with long pulse laser

To investigate the laser-plasma conditions for long pulse laser simulations were repeated using the code OSIRIS. The simulation results are displayed in terms of the normalised and Output frame from simulation are shown in the table 2 below.

Laser	Parameters	Plasma	Parameters
a_0	1.5	density	0.001 n_{cr} – 0.01 n_{cr}
spot diameter (FWHM)	10μm	target	Hydrogen gas
τ_L	30 ps	gas jet length	2mm

Table 2 Input parameters for the OSIRIS simulation

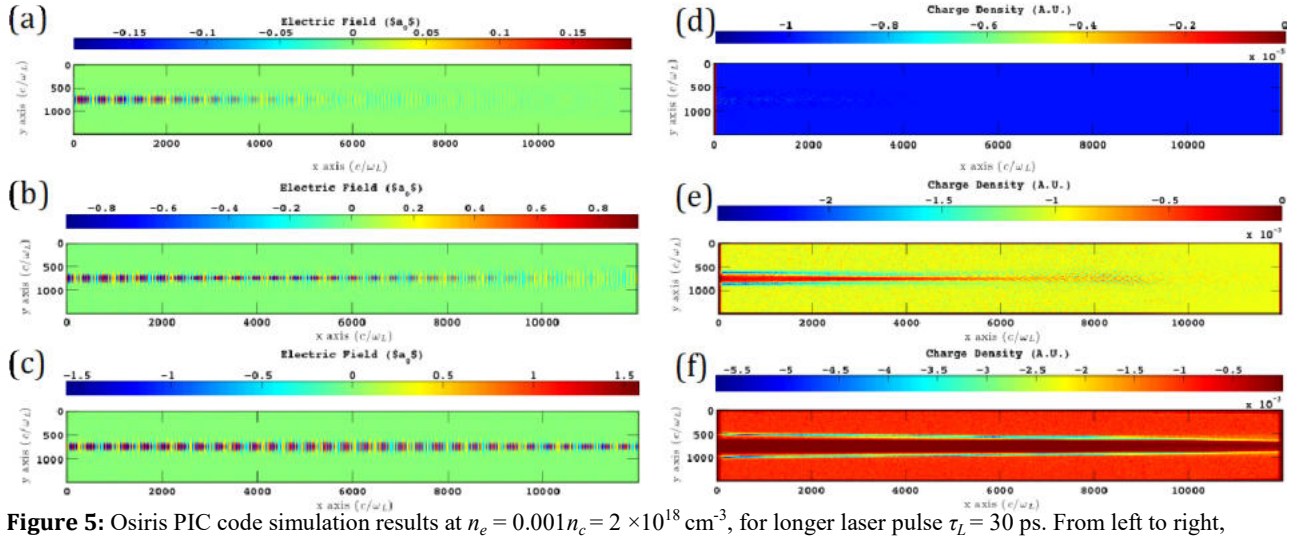

Figure 5: Osiris PIC code simulation results at $n_e = 0.001 n_c = 2 \times 10^{18}$ cm^{-3}, for longer laser pulse $\tau_L = 30$ ps. From left to right, transverse electric field and the electron number density. These are all shown for the same time step in the simulation from top to bottom, ~10 ps, 20 ps and 30 ps.

In the simulations, each box is approximately 25 mm in the y direction (transverse) and 1.581 mm in x (longitudinal), with a resolution of 12.56 cells/λ_0 in x and 6.28 cells/λ_0 in y. The time step between output was 0.49 ps and total simulated time was 30 ps. For the simulations presented, a stationary box was used to observe the plasma evolution following the passage of a laser pulse with a_0 = 1.5. The linearly polarised laser beam had a gaussian profile of 30 ps duration. In the simulations length and time are normalised to c/ω_0 = 0.16 (μm) and $1/\omega_0$ (= 0.059 fs), where ω_0 is the central laser frequency.

The simulations reveal that the formation of the channel progresses as follows. Initially, the laser beam remains focused over a relatively short distance given by the Rayleigh length. The ponderomotive force due to the laser, creates a plasma channel, which focuses the laser beam over a longer distance and overcome its divergence. Due to enhanced focusing, the length of plasma channel rapidly increases, which enhances beam focusing more and more. By this mechanism the laser is driven in a channel through the plasma, even though it is only mildly relativistic.

Figure 5 shows the transverse electric field and the electron density for t = 10 ps, t = 20 ps and t = 30 ps, respectively. The ponderomotive force of the laser expels all the electrons from the region of high intensity, leaving an ion channel as shown in figures. The electron densities after 10, 20 and 30 ps are shown in 5(b), 5(d) and 5(f). This shows that the electron density in the channel is close to zero. This electron cavitation was described by Sun et al. (15), (16). The expulsion of electrons is so strong that a shock-like structure is set up which expands away from the laser axis as shown in 5(f).

Simulations at higher electron densities have been also carried out up to n_e = 10^{20} cm^{-3}. But at these densities, the laser is rapidly depleted, thus obscuring the possible occurrence of channel creation as shown in figure 6.

In the simulation, after 24.5 ps, electrons have been accelerated up to $p = 20 m_e c$ (E ~3.5 MeV), with a small fraction extending to momenta as high as p = 120 $m_e c$ (E ~120 MeV), as evident in the p-x phase-space. The electrons in this case are clearly accelerated throughout the whole box and are not obviously bunched, as would be in the case of a classic wakefield acceleration process. Hence the likely mechanism by which they are accelerated is likely to be direct laser acceleration. Particularly noticeable is that there are no electrons accelerated beyond 10 MeV for the lowest density case now. Hence it appears that the complete cavitation that is observed in this case, completely suppresses the generation of very fast hot electrons. This is potentially good news for fast ignition applications since it would reduce the energy lost into very fast electrons, which play little role in the ignition process.

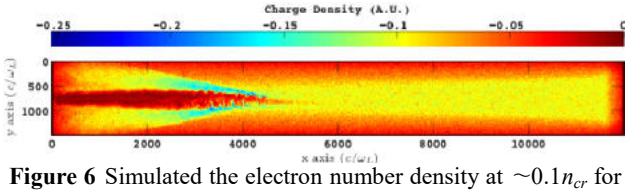

Figure 6 Simulated the electron number density at ~0.1n_{cr} for t ~30ps.

Conclusions

In conclusion, we have presented simulation observations of the propagation of high intensity 1ps and 30 ps laser pulses through hydrogen plasma. Here we have shown from the simulations that the formation of a straight, stable and long channel for low electron densities. At relativistic intensities, the ponderomotive

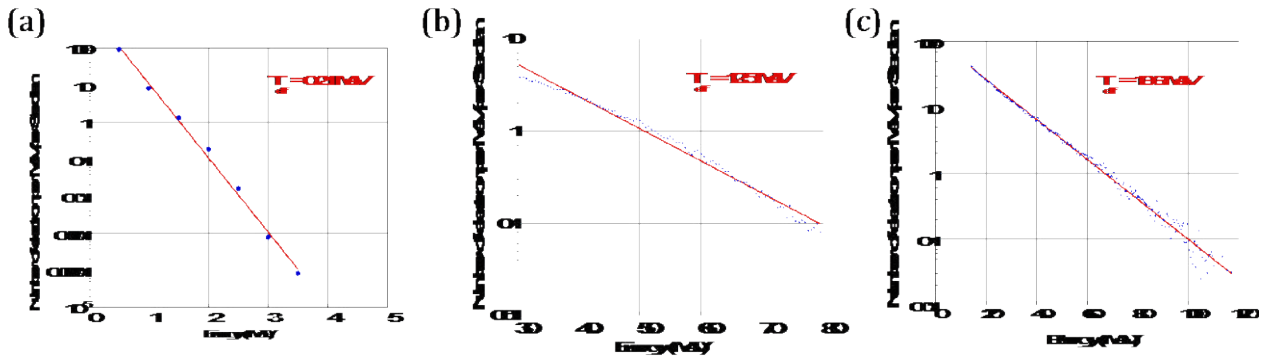

Figure 7: Figures (a), (b) and (c) show the given plasma density for $0.001n_{cr}$, $0.01n_{cr}$ and $0.1n_{cr}$ electrons, with a temperature fit for t ~30 ps.

force and relativistic effects will cause the laser pulse to self-focus. The generation of energetic electrons (100 MeV) was also observed in the case as short laser pulse, but with relatively little dependence on density. This also implies that the formation of the channel has the ability to reduce instabilities associated with the propagation. The observed characteristics of the channel have implications for both laser wake field accelerators and fast ignition inertial confinement fusion.

References

1. G. Li et al., Laser Channeling in Millimeter-Scale Underdense Plasmas of Fast-Ignition Targets. Physical Review Letters. 100:125002 (2008).
2. A. Modena et al., "Electron acceleration from the breaking of relativistic plasma waves. Nature Letters. 377:606 (2002).
3. S. Kneip et al., Observation of Synchrotron Radiation from Electrons Accelerated in a Petawatt-Laser-Generated Plasma Cavity. Physical Review Letters. 100:105006 (2008).
4. T.M Antonsen et al., Self-focusing and Raman scattering of laser pulses in tenuous plasmas. Physical Review Letters. 69:2204 (1992).
5. R. Kodama et al., Fast heating of ultrahigh-density plasma as a step towards laser fusion ignition. Nature. 412:798 (2001).
6. M. Tabak et al., Ignition and high gain with ultrapowerful lasers. Physics of Plasmas. 1:1626-1634 (1994).
7. N. Naseri et al., Self-channelling of relativistic laser pulses in large-scale underdense plasmas. Physics of Plasmas. 17:033107 (2010).
8. M. Borghesi et al., Relativistic Channeling of a Picosecond Laser Pulse in a Near-Critical Preformed Plasma. Physical Review Letters. 78:879 (1997).
9. J. Fuchs et al., Dynamics of Subpicosecond Relativistic Laser Pulse Self-Channeling in an Underdense Preformed Plasma. Physical Review Letters. 80:1658 (1998).
10. P. Kaw et al., Filamentation and trapping of electromagnetic radiation in plasmas. Physics of Fluids. 16:1522-1525 (1973).
11. V.K. Tripathi et al., Plasma effects in a free electron laser. Plasma Science, IEEE Transactions on. 18:466-471 (1990).
12. Z. Najmudin et al., Investigation of a channeling high-intensity laser beam in underdense plasmas. Plasma Science, IEEE Transactions on. 28:1057-1070 (2000).
13. A. Rehman et al., Formation of plasma channel with long pulse interaction. RAL CLF Annual Report. (2011).
14. S.P.D. Mangles et al., Electron Acceleration in Cavitated Channels Formed by a Petawatt Laser in Low-Density Plasma. Physical Review Letters. 94:245001 (2005).
15. G.Z. Sun et al., Self- focusing of short intense pulses in plasmas, and relativistic optical guiding. Physics of Fluids. 30:526(1987).
16. A. Pukhov et al., Laser wakefield acceleration:the highly non linear broken-wave regime. Applied. Phys. B. 74:355 (2002).

Dynamics of self-generated, large amplitude magnetic fields following high-intensity laser matter interaction

Contact *g.sarri@qub.ac.uk*

G. Sarri, X. H. Yang, S. Kar, M. E. Dieckmann, I. Kourakis, M.Borghesi

School of Mathematics and Physics, The Queen's University of Belfast, Belfast, BT7 1NN, UK

C.A. Cecchetti

Light4Tech s.r.l, 50018 Scandicci, Italy

A. Macchi, F. Pegoraro

Dipartimento di Fisica "E. Fermi", Largo B. Pontecorvo 3, I-56127 Pisa, Italy

T. V. Liseykina

Institut fur Physik, Universitat Rostock, D-18051 Rostock, Germany

L. Romagnani, J. Fuchs

LULI, Ecole Polytechnique, CNRS, CEA, UPMC; 91128 Palaiseau, France

M. Galimberti, A. P. L. Robinson

Rutherford Appleton Laboratory, Central Laser Facility, Chilton, OX11 0QX, UK

J. Osterholz, R. Jung, O. Willi

Institute for Laser and Plasma Physics, Heinrich Heine University, Dusseldorf, Germany

Introduction

Magnetic fields have been studied in laser-produced plasmas since the introduction of high-power lasers, with emphasis on their role in Inertial Confinement Fusion [1]. This regime has been characterized in detail only recently by temporally and spatially resolved measurements [2]. In the case of short (~ps) and intense ($I_L \geq 10^{18}$ Wcm^{-2}) laser pulses, hot electrons may drive the generation of very intense magnetic fields either by driving Weibel-like instabilities [3] or by recirculation at the boundary of the laser-plasma (fountain effect) [4]. Previous experimental work has detected effects induced by such magnetic fields on external optical beams [5] or on the polarization of self-generated harmonics [6]. However, these measurements suffered of limitations, in terms either of the range of plasma density accessible [5] or of spatial and temporal resolution [6]. We report here on simultaneous measurements of the magnetic fields generated at the front and at the rear side of a solid target irradiated by a short and intense laser pulse, using a proton imaging technique [7]. Data analysis gives evidence of the generation of toroidal magnetic fields (B_{MAX} ~ 50 MegaGauss) that decay in time on a ps time scale. They are consistent with the recirculation of the laser-accelerated electrons around the target and are able to confine the radial expansion of the plasma.

Experimental setup and data analysis

The experiment was carried out using the Vulcan laser system at the Rutherford Appleton Laboratory [8] using two laser beams ($\lambda \sim 1\mu m$, E_L=50J, τ_L=1ps, preceded by a lower intensity plateau $I_P \sim 10^{12}$ Wcm^{-2}, τ_P=300 ps). The first laser beam (CPA_1 in Fig.1) was focused to a peak intensity of $I_L \sim 10^{19}$ Wcm^{-2} onto a d=10μm thick Al foil, with a 45 degrees angle of incidence. Hydrodynamic simulations indicate that the laser pre-pulse induces a pre-plasma with a scale-length of 2.5 microns and an electron temperature of 100 eV. The second laser beam (CPA_2 in Fig.1) was focused onto a 20μm thick gold foil to generate a proton beam with cut-off energy of approximately 20 MeV. This beam was used as a charged-particle probe [7] and was recorded onto a stack of calibrated RadioChromic Films (RCFs) [9] giving a point-like projection of the interaction. Previous theoretical modeling of high-intensity irradiation of thin solid targets [10] indicates the generation of magnetic fields having a toroidal structure with azimuthal symmetry with field lines parallel to the target surface. In the present experiment, in order to maximize the probe protons deflections due to magnetic fields over those due to electric fields, the propagation axis of the probe beam was chosen to be normal to the target surface. Two configurations were adopted: the proton beam first encountered either the rear, un-irradiated side of the target (direct configuration, Fig.1.a) or the front, irradiated side (reverse configuration, Fig. 1.g). A typical set of RCF images, obtained in the direct configuration, is displayed in Figs. 1 b-e. All images depict the presence of two main features: an outer ring (radius of the order of 100 - 200 μm) and an inner dot (radius of the order of 30-40 μm) of proton accumulation. The outer ring slowly expands in time whilst roughly preserving its amplitude whereas the inner dot shrinks and eventually disappears as time progresses. Radiographies obtained in the reverse configuration (Figs. 1 h-k) show an inverse deflection pattern, as expected for magnetic deflections. For a quantitative analysis of the magnetic field, Particle Tracer (PT) [11] simulations have been performed. The radius and depth of the distribution and the maximum amplitude of the magnetic fields at both sides of the target have been varied in order to best match the proton deflections pattern observed for each probing time. A comparison between the experimental and simulated pattern is shown in Fig. 2. By iteratively applying this method to each RCF layer, it has been possible to extract the temporal evolution of the magnetic fields at each side of the target (Fig. 3).

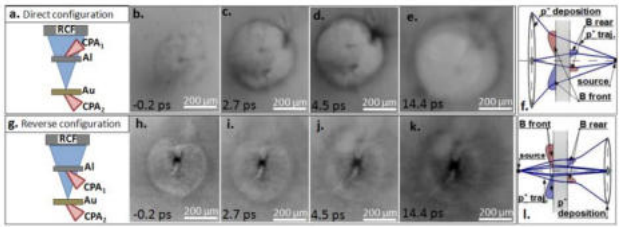

Fig. 1 b. – e. Proton imaging data at ~ -0.2, 2.7, 4.5, 14.4 ps after the peak of the CPA_1 pulse in the direct configuration (sketched in the frame **a.**) **f.** Sketch of the proton deflections induced by the magnetic fields in the direct configuration. **h. – k.** Proton imaging data at ~ -0.2, 2.7, 4.5, 14.4 ps after the peak of the CPA_1 pulse in the reverse configuration (sketched in the frame **g.**) **l.** Sketch of the proton deflections induced by the magnetic fields in the reverse configuration.

Numerical modeling

The generation of magnetic fields of several tens of MegaGauss at both sides of the target and with opposite polarity, is also supported by two-dimensional (2D) Particle-In-Cell (PIC) simulations. A density profile composed by an exponential ramp reproducing the above mentioned preplasma, followed by a plasma bulk with electron density $n_e=40n_c$ and charge-to-mass ratio Z/A=9/26 is assumed. The laser pulse has a Gaussian transverse profile (FWHM = 5μm), a duration of 250T

(T=3.3fs), dimensionless peak amplitude a_0 = 2.7, and it is incident at 20 degrees with respect to the normal of the target surface.

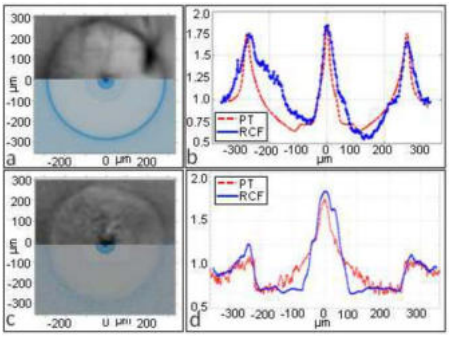

Fig. 2 Comparison between the experimental proton dose deposition as recorded by the RCF and that resulting from PT simulations for the direct (frames **a.** and **b.**) and reverse (frames **c.** and **d.**) configuration.

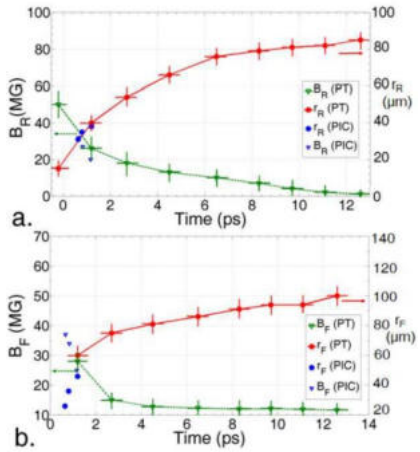

Fig. 3 Temporal evolution of the magnetic field amplitude and width at the rear (**a.**) and front (**b.**) side of the target as extracted from matching PT simulations, compared with the PIC results. Time refers to the peak of the laser pulse.

The simulation ran for 600T ~ 2 ps. Fig. 4 shows the generation of magnetic fields at the front and rear edges of the target in agreement with the experimental findings (see Fig. 3). In principle, strong magnetic fields may also be generated inside the target due to resistive return currents which must balance the fast electron flow.

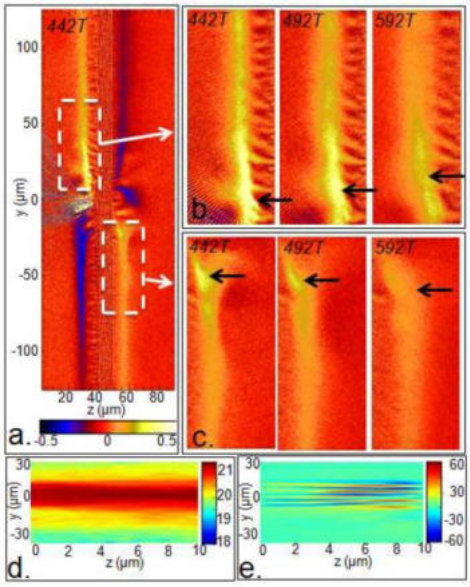

Fig. 4 a.- c.: PIC simulation results. The frames show the transverse magnetic field t=442 T in units of B_0= 107 MG (**a.**), and a zoom of the front (**b.**) and rear (**c.**) regions corresponding to the dashed rectangles in **a.** at t=442, 492 and 592 T. The black arrows indicate the position of the field maxima. **d.- e**: transport simulation results. The frames show the hot electron density inside the target in logarithmic scale and units of cm^{-3} (**d.**) and the related magnetic field distribution in units of MG (**e.**), both at t=1 ps after the peak of the pulse.

However, 3D simulations of the propagation of an electron beam through Aluminium at an initial temperature of 1 eV (using the code ZEPHYROS [12]), show the growth of small-scale filaments with magnetic fields amplitude up to 40MG and a characteristic spatial scale of 4μm (Fig. 4.e) which is below the proton imaging resolution [7].

It is thus reasonable to assume that, in these specific experimental conditions, the proton deflections are induced exclusively by the magnetic fields generated outside the target.

Analytical modeling

The hot electron temperature is T_h ~ 0.6MeV, corresponding to a velocity v_h ~ 0.9 c; the hot electron density may be thus roughly estimated by $f I_L=n_h v_h T_h$ yielding, for an absorption fraction f~0.1 [13], n_h~$4x10^{20}cm^{-3}$. The total current may be estimated as $I_h=en_h v_h S$ ~ 5 x 10^6A, where S~$3x10^{-6}$ cm^2 is the area of the focal spot. The divergent flow of the hot electrons allows part of the current to flow in the radial direction forming loops which fall back to the target where a surface return current may close the circuit. A simple geometrical model [14] of such *fountain effect* indicates B_{MAX}~$\alpha\theta B_0$, where $B_0=\mu_0 I_h/(2\pi r_0)$, θ~25 degrees is the divergence of the flow, r_0 ~ 15 μm is the radius of the electron emitting area and $\alpha \sim 8T_h/(eEr_0)$ with E the typical value of the electric field. PIC simulations indicate E~10^{12} V/m; we thus obtain a peak value of 70 MG, in agreement with the experimental results. In these conditions, the magnetic field tends to confine the plasma. The magnetic energy density ($u_m=B^2/2\mu_0=4x10^5B^2_{10}$ Jcm^{-3}) becomes in fact comparable to the plasma thermal energy (u_t ~ $4x10^7$ Jcm^{-3}).

Conclusions

In conclusion, temporally and spatially resolved proton imaging indicates the generation of toroidal magnetic fields of tens of MegaGauss on both sides of a laser-irradiated target. Our results suggest that the magnetic field can play an important role in ion acceleration in the expanding sheath, and should be taken account in related modeling. The self-confining effect also qualitatively resembles the collimation of leptonic astrophysical jets.

Acknowledgements

We acknowledge the support of the RAL-CLF staff. This work was supported by EPSRC [Grant Numbers EP/E035728/1 (LIBRA consortium), EP/D06337X/1 and EP/J002550/1], by British Council-MURST-CRUI, by a Leverhulme Trust fellowship (ECF-2011-383), and by the VSR of the Research Center Julich under the project HRO01.

References

1. J. Stamper *et al.*, Phys. Rev. Lett. **40**, 1177 (1978).
2. C. A. Cecchetti *et al.*, Phys. Plasmas **16**, 043102 (2009); R. D. Petrasso *et al.*, Phys. Rev. Lett. **103**, 085001 (2009); J. R. Rygg *et al.*, Science **319**, 1223 (2008); L. Willingale *et al.*, Phys. Rev. Lett. **105**, 095001 (2010).
3. U. Wagner *et al.*, Phys. Rev. E **70**, 026401 (2004).
4. Y. Sakagami *et al.*, Phys. Rev. Lett. **42**, 839 (1979).
5. M. Borghesi *et al.*, Phys. Rev. Lett. **81**, 112 (1998).
6. M. Tatarakis *et al.*, Nature **415**, 280 (2002).
7. G. Sarri *et al.*, New J. Phys. **12**, 045006 (2010).
8. C. N. Danson et al., J. Mod. Opt. **45**, 1653 (1998).
9. J.F.Dempsey *et al.*, Med. Phys. **27**, 2462 (2000).
10. A. Pukhov, Phys. Rev. Lett. **86**, 3562 (2001).
11. L. Romagnani, Ph.D. thesis,The Queen's University of Belfast, Belfast, U.K., 2005.
12. S. Kar *et al.*, Phys. Rev. Lett. **102**, 055001 (2009).

13. J. Fuchs *et al.*, Nat. Phys. **2**, 48 (2006).

14. A. Macchi, ArXiv: 1202.0389v1 (2012).

Controlling Fast-Electron Beam Divergence Using Two Laser Pulses

R.H.H. Scott,[1,2,*] C. Beaucourt,[3] H.-P. Schlenvoigt,[4] K. Markey,[2] K.L. Lancaster,[2] C.P. Ridgers,[5] C.M. Brenner,[6,2] J. Pasley,[7] R.J. Gray,[6] I.O. Musgrave,[2] A.P.L Robinson,[2] K. Li,[8] M.M. Notley,[2] J.R. Davies,[8] S.D. Baton,[4] J.J. Santos,[3] J.-L. Feugeas,[3] Ph. Nicolaï,[3] G. Malka,[3] V.T. Tikhonchuk,[3] P. McKenna,[6] D. Neely,[2,6] S.J. Rose,[1] and P.A. Norreys[1,2]

[1]*Department of Physics, The Blackett Laboratory, Imperial College London, Prince Consort Road, London, SW7 2AZ, United Kingdom*
[2]*Central Laser Facility, STFC, Rutherford Appleton Laboratory, Harwell Oxford, Didcot, OX11 0QX, United Kingdom*
[3]*Univ. Bordeaux/CNRS/CEA, CELIA, UMR 5107, 33405 Talence, France*
[4]*LULI, École Polytechnique, UMR 7605, CNRS/CEA/UPMC, Route de Saclay, 91128 Palaiseau, France*
[5]*Clarendon Laboratory, University of Oxford, Parks Road, Oxford OX1 3PU, United Kingdom*
[6]*SUPA, Department of Physics, University of Strathclyde, Glasgow, G4 0NG, United Kingdom*
[7]*Department of Physics, University of York, York, YO10 5DD, United Kingdom*
[8]*GoLP, Instituto de Plasmas e Fusão Nuclear - Laboratório Associado, Instituto Superior Técnico, 1049-001 Lisboa, Portugal*

(Dated: July 4, 2012)

This paper describes the first experimental demonstration of the guiding of a relativistic electron beam in a solid target using two colinear, relativistically intense, picosecond laser pulses. The first pulse creates a magnetic field that guides the higher-current fast-electron beam generated by the second pulse. The effects of intensity ratio, delay, total energy and intrinsic prepulse are examined. Thermal and K_α imaging show reduced emission size, increased peak emission and increased total emission at delays of $4-6$ ps, an intensity ratio of $10:1$ (second:first) and a total energy of 186 J. In comparison to a single, high-contrast shot, the inferred fast-electron divergence is reduced by 2.7 times, while the fast-electron current density is increased by a factor of 1.8. The enhancements are reproduced with modeling and are shown to be due to the self-generation of magnetic fields. Such a scheme could be of considerable benefit to fast ignition inertial fusion.

The study of fast-electron transport in high-density plasmas is important for numerous applications including proton and ion beam production [1], isochoric heating of high density matter for opacity studies [2], and fast-ignition inertial fusion [3].

Electron-driven fast-ignition is a promising alternative route to inertial confinement fusion, albeit much less developed than the central hot-spot ignition approach. The efficiency of laser energy coupling to the DT fuel is determined by the fraction of energy absorbed into the fast-electrons, their temperature, divergence, and the distance from the critical surface to the compressed core [4]. The electron beam divergence, which is addressed here, can be controlled by target manufacturing techniques [5, 6]; however these have a significant impact on the target complexity and cost.

This letter describes an experimental investigation of a theoretical scheme proposed by Robinson *et al.* [7] to reduce the fast-electron divergence using two laser pulses. The first (lower intensity) pulse accelerates electrons into the target, generating an azimuthal magnetic field within the target. The second laser pulse then accelerates the main fast-electron population into the target. If the pre-generated magnetic field is of sufficient magnitude and correct geometry, the divergent main electron population is deflected towards the beam axis, thereby reducing the divergence and further reinforcing the magnetic field.

In addition to generating magnetic fields, the first pulse alters the target front surface, affecting the laser-plasma interaction of the main pulse. Particle-in-cell (PIC) modeling shows the first laser pulse is sufficiently intense and energetic to hole-bore through the underdense plasma ablated by the pulse's leading edge, heating it to temperatures of $\sim$ 1 keV [8, 9]. This will cause the front surface to expand during the delay between the pulses.

Previous work by Yu *et al* [10] showed (using PIC modeling) that multiple pulses can hole-bore more effectively than an equivalent single-pulse in a plasma with a density twice the critical density, $n_e \simeq 2\,n_c$. The generation of magnetic fields by using two pulses in a solid target was previously attempted experimentally by Norreys *et al* [11]. The null results were attributed to insufficient current from the first pulse and detrimental effects caused by a prepulse. Markey *et al* [12] increased the efficiency of proton acceleration by using two pulses. This was attributed to the combined effects of absorption enhancement and a two-stage rear-surface acceleration process, yielding an optimal pulse delay of 1.5 ps.

The experiment reported here provides the first experimental evidence for electron beam guiding in a solid target by using two laser pulses. It was performed using the Vulcan petawatt laser at the Central Laser Facil-

ity, Rutherford Appleton Laboratory [13]. The 1054 nm laser pulse contained 186±11 J (except shot t_{delay} = 7 ps (the temporal delay between the two pulses) which had +28 J) of energy on target, with 20% of that energy contained within a focal spot of 7 μm full-width-at-half-maximum (FWHM) in a duration of 1.4±0.3 ps, yielding a peak intensity of $\sim 1.0 \times 10^{20}$ W/cm^2. A new picosecond OPCPA front end [14] gives intensity contrast $\sim 10^{-10}$ and energy contrast $\sim 10^{-7}$, the low-contrast front end used for selected shots had an energy contrast of 8×10^{-5}. The Al(75 μm)Cu(10 μm)Al(1 μm) layered planar targets (transverse dimensions 5 mm) were shot (on the thicker Al layer) at 45° p-polarisation.

Two laser pulses were created by passing the incident beam through a half-wave plate and then a polarising beam cube. The wave plate angle controls the relative pulse levels (R=I_2:I_1) where I_1 is the intensity of the first pulse on target. Roof prisms retroreflected both pulses, and the temporal delay between the two pulses (t_{delay}) was altered by translating one prism. The polarisations of the pulses were matched, before recombination in a nonpolarising cube. By interfering 100 fs pulses from the seed oscillator, the pulses were synchronised to within 50 fs. Calibration ensured that the sum of the energy in both pulses was constant regardless of t_{delay}.

The target rear-surface temperatures were measured using Cu K$_\alpha$ x-ray spectroscopy and streaked pyrometry of the rear-surface. A KAP conical crystal with 2D spacing of 26.64 Å focussed the $6.85 - 8.5$ keV x-rays (including the Cu K$_{\alpha_1}$ and K$_{\alpha_2}$ lines) onto a FUJI BAS image plate [15]. Bulk electron temperatures within the Cu fluor layer were inferred by fitting Cu K$_{\alpha_1}$ and K$_{\alpha_2}$ line spectra generated by the non-LTE code FLYCHK [16] to the data. F/5.3 optics at 59° from target normal collected the visible optical emission from the target rear-surface, which was split between a spectrometer and a high-speed sampling camera (HISAC)[17], the latter gave 2D spatial (24 μm) and temporal resolution ($\sim$ 50 ps) and multiframe capability (1 ns window). The Plankian thermal radiation signal was separated from the prompt optical transition radiation (OTR) signal[18], by extracting the measurement 100 ps after the laser interaction - when the OTR signal has decayed. Radiation-hydrodynamic modeling was used to back-out the initial target temperature based on the total thermal emission at t=100 ps. HYADES [19] was used to model the target hydrodynamic expansion and cooling, and the resultant evolution of the rear-surface thermal spectrum during the 100 ps delay. The time-varying thermal spectrum was folded with the spectral response of the streak camera optics, tube and spectral filtering, then spectrally integrated giving the emission intensity as a function of time for a given initial target temperature. By changing the initial target temperature, a family of intensity-time curves was generated, relating the initial target temperature to the measured intensity at t=100 ps. An absolutely calibrated lamp provided a reference intensity. The measured thermal emission image is caused by the fast-electrons heating the target via collisional and collective mechanisms.

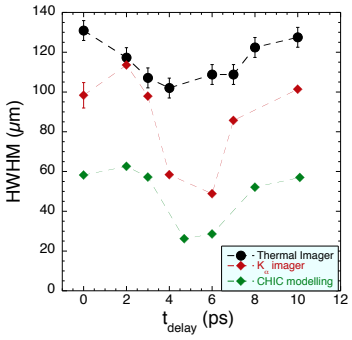

Figure 1. Dependence of the HWHM of the Cu K$_\alpha$ (red diamonds) and thermal emission images (dots) from the rear-surface on the time delay between laser pulses. For the data at zero time delay the mean has been calculated and the standard deviation provides the error bar. The lower curve (green diamonds) shows the results of numerical simulations, this reproduces the delay required for optimal collimation.

The fast-electron spatial distribution was measured in a 10 μm Cu fluor layer 1 μm beneath the target rear-surface. A spherically bent quartz $21\bar{3}1$ crystal imaged the Cu K$_\alpha$ emission (caused by fast-electron collisions) onto a FUJI BAS image plate.

The half-width-at-half-maximum (HWHM) of the Cu K$_\alpha$ and thermal emission spot sizes as a function of t_{delay} are shown in figure 1. For the optimal t_{delay}= $4 - 6$ ps, the size of the K$_\alpha$ emission is halved, while the thermal emission is reduced by 25%. The HWHM of the single-pulse Cu K$_\alpha$ images increased linearly with target thickness, with a half angle of 42.0° and source size of 26 µm. Based on this source size, the half angle for t_{delay}= 6 ps was reduced to 15.4° - a reduction of 2.7 times.

The differences between the Cu K$_\alpha$ x-ray and thermal imaging diagnostics results depicted in figure 1 are attributed to the thermal signal being extracted 100 ps after the initial interaction - conductivity within the target will increase the thermal emission size over this time.

Figure 2 illustrates the change in the fast-electron beam profile induced by the double-pulse. The enhancements in the peak height and reduction in width when using the optimal parameters are clear from the double-pulse shot with t_{delay}=6ps (DP), even when compared to the best single-pulse shot using Vulcan's new picosecond OPCPA high-contrast front end (HC1). A comprehensive examination of the effect of the new high-contrast front end was performed by bypassing it during the experiment, reverting to the pre 2010 lower contrast [20]. Shot LC was a typical example of Cu K$_\alpha$ imager data using a single, low-contrast pulse; the background subtracted peak flux is enhanced by $\sim$ 5.5× when the double-pulse

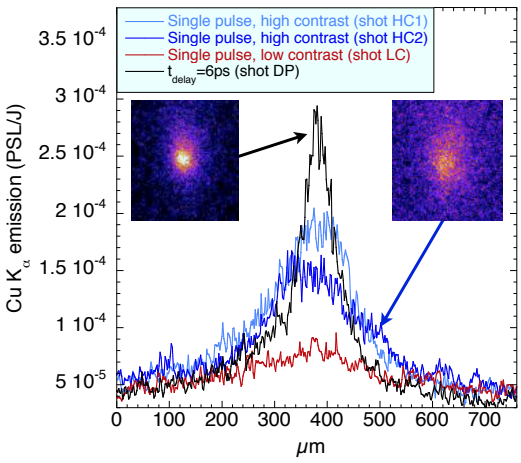

Figure 2. Examples of lineouts from the Cu K_α imager: Shots HC1 and HC2 depict the best and typical high-contrast shots respectively, comparison with shot LC, which is a typical low-contrast shot, illustrates the reduction in K_α spatial HWHM and increase in peak signal with increasing laser contrast. Shot DP is the optimal double-pulse shot with t_{delay}=6 ps, in comparison with the high-contrast data the K_α HWHM is halved while the background subtracted peak signal is increased by a factor of 1.8. Inset are two Cu K_α images with the same spatial brightness scales, showing shots HC2 and DP.

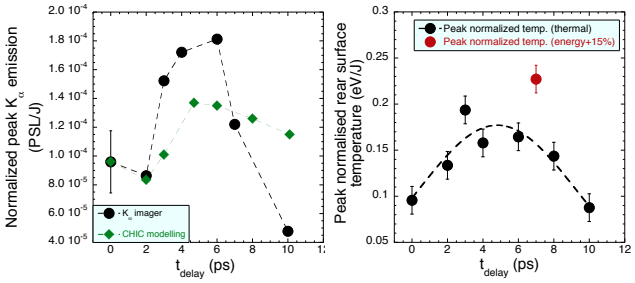

(a) (b)

Figure 3. (a) Dependence of the peak Cu K_α emission (normalised to the laser energy on target) on the time delay obtained in the experiment (dots) and in simulations (green diamonds). The error bar at zero delay depicts the standard deviation. The modelled data is normalised to the emission at 0 ps. (b) Dependence of the peak rear-surface temperatures derived from the thermal emission normalised to the laser energy on target. The data points are fitted with a Gaussian distribution. The shot in red had 15% more energy on target than the mean, but 2.2 times higher temperature than a single-pulse shot.

is used with t_{delay}= 6 ps. It should be emphasised that this was also the first experimental implementation of the new high-contrast front end on Vulcan TAP, meaning in one experiment the peak Cu K_α flux has been increased by $\sim 5.5\times$ over the previous state-of-the-art.

Figure 3 (a) depicts the peak Cu K_α imager emission normalised to laser energy on target - an approximate measure of relative fast-electron current density. The peak K_α emission is increased in the range t_{delay} = 3-7 ps, at 6 ps the value is 1.9 times that of a single-pulse. Figure 3 (b) shows laser energy normalised target rear-surface temperatures. The optimal delay for both the peak Cu K_α imager emission and the thermally derived target rear-surface temperatures corresponds with the optimal HWHM (figure 1). The mean rear-surface temperature derived from Cu K_α spectroscopy was 25.8 eV or 0.139 eV/J (standard deviation 0.028) - very similar to that of the thermal data.

When the energy in the first pulse was halved - both by halving the total energy (90 ±16 J) and keeping R=10:1, or by switching to R=20:1 (182 ±20 J) - no evidence of collimation was observed. The laser energy on the nominal shots was within 6% of the mean except shot t_{delay}= 7 ps which had 15% higher energy than the mean, interestingly the laser energy normalised rear-surface temperature (figure 3(b)) is increased by a factor of 2.2 over the single-pulse high-contrast shot - considerably more than the other double-pulse shots. This indicates that with more energy on target the gains due to the two pulse scheme may scale non-linearly with energy.

The experiment was modelled using the 2D radiation hydrodynamics code CHIC [21] using MHD and fast-electron transport modules. Magnetic fields are generated by the resistive electric field and the cross product of the gradients of the electron density and temperature, while the electric field is calculated assuming total current neutralisation. The plasma resistivity was described by the Spitzer formula above ~ 100 eV and by an interpolation formula [22] below. fast-electron transport is modelled with a reduced kinetic model [23, 24] which includes self-consistent magnetic fields and collisions with plasma electrons and ions. The intensity of Cu K_α emission was calculated with a postprocessor.

Two temporally separated electron populations were injected into a 80 μm thick Al target. Both electron beams have the same duration of 2 ps FWHM. Their radial profiles at the front side were Gaussian distributions of FWHM 34 μm and order 0.7 (i.e. $exp[-(r/R_0)^{(2x0.7)}]$). The energies in the first and second electron beams were 1.2 J and 15 J. This accounts for 20% of the laser energy within the focal spot and absorption fractions of 33% and 42% for the first and second beams, respectively. The energy distribution of fast-electrons were Maxwellian with temperatures of 0.6 MeV and 2.75 MeV calculated by taking the maximum of either Beg or ponderomotive scaling laws. The angular distribution at the source was chosen according to Ref. [25] with a half angle divergence of 35° and the dispersion angle 45°.

As shown in figure 1, the modeling and experiment both have a factor of two decrease in the K_α emission HWHM with respect to the diameter from the single-

pulse shot, the minimum HWHM also occur with t_{delay} = 4-6 ps. In both the experiment and model for t_{delay} > 6 ps the HWHM increases back to the single-pulse value. The minimum in the HWHM corresponds with a modelled peak magnetic field of 0.45 MG, for larger delays the magnetic field diffuses away from the propagation axis, reducing in magnitude. We note that in both the experiment and modeling, in comparison to the 0 ps case, the 2 ps delay has a slightly increased K_α HWHM. This is because in the 2ps case, t_{delay} is of the order of the pulse duration, meaning the fast-electron beam is effectively one longer pulse with reduced current in comparison to the 0 ps case. In this resistivity/temperature regime, the lower current of the 2 ps case generates a smaller magnetic field meaning the electron beam is less well guided. Differences in the absolute size from model to experiment may be due to differences between the modelled and experimental spatial distributions of the injected electrons. Experimentally, 20% of the total laser energy is contained within the focal spot FWHM and 50% is contained within a 16 µm spot diameter [26]. Only the energy within the focal spot is modelled which may explain the differences between the experimental and modeling results. Note that reproduction of the experimental results required a modelled electron spatial distribution with 'wings', this fits with the laser energy spatial distribution.

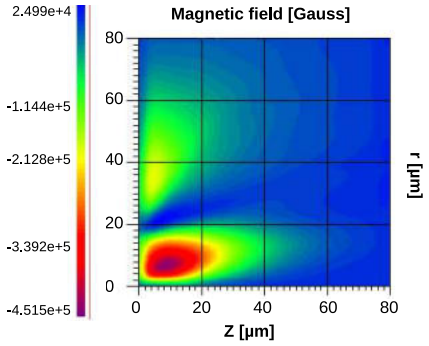

Figure 4. The modelled magnetic field at the time when the second pulse is beginning for the case where the guiding was optimal (t_{delay} = 4.7 ps). The negative field near the axis collimates the fast-electrons.

The main features of the observed fast-electron transport are explained as follows: (1) the first laser pulse 'injects' a population of fast-electrons into the target which seed an azimuthal magnetic field, the energy density of which is proportional to the radial derivative of the electron beam current density. On axis the induced magnetic field acts to collimate the injected fast-electrons, while at larger radii the sign of the magnetic field reverses, causing the injected fast-electrons to diverge. (2) The induced magnetic field increases in magnitude until approximately the end of the first pulse and moves deeper into the target. Then it diffuses radially reducing in magnitude. (3) If the second electron population arrives too early or the current in the first pulse is too small, the generated magnetic field is insufficient and the beam less well guided. This explains why no collimation is observed for small t_{delay}, when the total energy on target is reduced and when the first pulse energy on target is reduced (R=20:1). (4) At the optimal delay, the magnetic field is at a maximum and the majority of the injected fast-electrons interact with the convergent region of the magnetic field. In this case the optimal collimation of the beam occurs. In the case where the energy on target was higher (t_{delay} = 7 ps), the current is higher meaning the magnetic field is larger and the guiding more effective. (5) The optimal delay is exceeded when the radial field diffusion is such that the collimating magnetic field is too weak to collimate the injected fast-electrons, hence little guiding occurs and the beam is relatively unaffected.

In summary, the first evidence has been provided that two laser pulses of total energy 186 J, energy ratio 10:1 and time delay of $4-6$ ps yield optimised electron beam guiding characteristics. In comparison to single-pulse shots the optimised fast-electron beam has the following parameters: K_α imager HWHM ×0.5, peak K_α imager signal vs high (low) contrast single-pulse ×1.8 (×5.5), peak thermally derived rear-surface temperatures ×2. Modeling accurately reproduces this data showing that a magnetic field generated within the target by the first pulse acts to collimate the second pulse. Under the optimal conditions the beam divergence is reduced by a factor of 2.7 with the fast-electrons generated by the main laser pulse being guided over a distance of 80 μm. This experimental evidence shows that the fast-electron beam characteristics can be *significantly* enhanced over the previous state-of-the-art, improving many of the fast-electron beam parameters critical for fast ignition inertial confinement fusion and many other applications of intense laser-solid interactions.

* Robbie.Scott@stfc.ac.uk; The authors gratefully thank the staff of the Central Laser Facility, STFC Rutherford Appleton Laboratory, the Aquitaine Regional Council and A.R. Bell for useful discussions. This investigation was undertaken as part of the HiPER preparatory project and was funded by the UK Science and Technology Facilities Council.

[1] E. L. Clark *et al.*, Phys. Rev. Lett. **84**, 670 (2000).
[2] D. Hoarty *et al.*, High Energy Density Phys. **3**, 115 (2007).
[3] M. Tabak *et al.*, Phys. Plasmas **1**, 1626 (1994), part 2.
[4] S. Atzeni and M. Tabak, Plasma Phys. & Controlled Fusion **47**, B769 (2005).
[5] R. B. Campbell *et al.*, Phys. Plasmas **10**, 4169 (2003).
[6] A. P. L. Robinson and M. Sherlock, Phys. Plasmas **14**, 083105 (2007).
[7] A. P. L. Robinson, M. Sherlock, and P. A. Norreys, Phys. Rev. Lett. **100**, 025002 (2008).

[8] W. Theobald *et al.*, Phys. Plasmas **13**, 043102 (2006).
[9] J. J. Santos *et al.*, Phys. Plasmas **14**, 103107 (2007).
[10] W. Yu *et al.*, Laser and Particle Beams **27**, 109 (2009).
[11] P. Norreys *et al.*, Nuclear Fusion **49**, 104023 (2009).
[12] K. Markey *et al.*, Phys. Rev. Lett. **105**, 195008 (2010).
[13] C. Danson *et al.*, Nuclear Fusion **44**, S239 (2004).
[14] I. Musgrave *et al.*, Appl. Opt. **49**, 6558 (2010).
[15] A. L. Meadowcroft, C. D. Bentley, and E. N. Stott, Review of Scientific Instruments **79**, 113102 (2008).
[16] H.-K. Chung *et al.*, High Energy Density Physics **1**, 3 (2005), ISSN 1574-1818.
[17] R. Kodama, K. Okada, and Y. Kato, Review of Scientific Instruments **70**, 625 (1999).
[18] S. D. Baton *et al.*, Phys. Rev. Lett. **91**, 105001 (2003).
[19] N. C. Woolsey *et al.*, Phys. Rev. E **57**, 4650 (1998).
[20] I. O. Musgrave *et al.*, Appl. Opt. **46**, 6978 (2007).
[21] J. Breil and P.-H. Maire, Journal of Computational Physics **224**, 785 (2007), ISSN 0021-9991.
[22] B. Chimier, V. T. Tikhonchuk, and L. Hallo, Phys. Rev. B **75**, 195124 (2007).
[23] Dubroca, B., Feugeas, J.-L., and Frank, M., Eur. Phys. J. D **60**, 301 (2010).
[24] Ph. Nicolaï *et al.*, Phys. Rev. E **84**, 016402 (2011).
[25] A. Debayle *et al.*, Phys. Rev. E **82**, 036405 (2010).
[26] P. K. Patel *et al.*, Plasma Phys. & Controlled Fusion **47**, B833 (2005).

X-ray Scattering from Warm Dense Iron

Contact swhite06@qub.ac.uk

S. White, G. Nersisyan, T.W.J. Dzelzainis, B. Kettle,
K. McKeever, C.L.S. Lewis and D. Riley
Centre for Plasma Physics, Queen's University Belfast
University Road, Belfast, BT7 1NN, UK

T. White and G. Gregori
Clarendon Laboratory, University of Oxford
South Parks Road, Oxford, OX1 3PU, UK

A. Otten, K. Siegenthaler, D. Kraus and M. Roth
Institut für Kernphysik, TechnischeUniversität Darmstadt
Schlossgartenstr. 9, 64289 Darmstadt, Germany

K. Wünsch, J. Vorberger and D.O. Gericke
Centre for Fusion, Space and Astrophysics, University of Warwick,
Gibbet Hill Road, Coventry, CV4 7AL

Introduction

Warm Dense Matter (WDM) is an intermediate state of matter, characterized as being too dense (approx solid density) to be described as weakly coupled plasma, too hot (0.1-10 eV) for condensed matter physics and usually exhibiting partial electron degeneracy[1].

A key parameter, often used to define WDM, is the ion-ion coupling parameter, which in c.g.s. units is;

$$\Gamma_{ii} = \frac{(Z^* e)^2}{a_{ii} k_b T_i} .$$

Z^* is the average ionization, a_{ii} is the Wigner-Seitz radius and the other quantities have their usual meaning. $\Gamma_{ii} \geq 1$ delineates the WDM region in plasmas.

WDM occurs in inertial confinement fusion experiments, in astrophysical plasmas, for example, in cool dense stars and the interiors of large planets. Indeed, this last point is the motivation behind this particular study.

Iron is believed to constitute the bulk of material present in the Earth's core. Figure 1 shows a proposed phase diagram for iron. At the boundary between the solid inner core and liquid outer core the conditions are believed to be approximately 6000-8000 K, 330 GPa and 13 g/cm^3 [2]. This is well above the normal evaporation temperature of iron (3134 K) and thus the iron is believed to be in a WDM state.

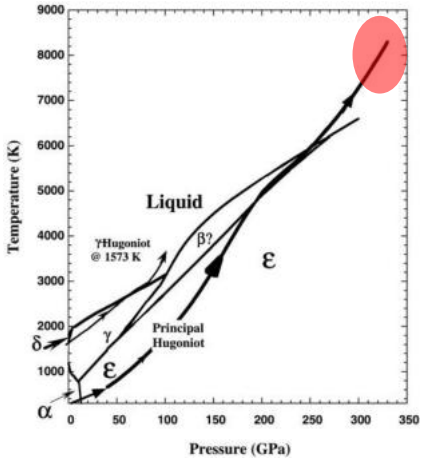

Figure 1. Proposed phase diagram for pure Iron [3]. Red shaded region shows probable core conditions.

Accurate models for iron under these extreme conditions are therefore essential for describing, not only the interiors of Earth, but also those of the many so-called "super-Earths" that have been discovered in the last twenty years. The melt curve for iron is still uncertain and the lack of accurate equation of state data in this regime affects the interpretation of gravitational moments and total mass measurements.

One method that has proven very successful to probe such high density material is to use x-ray scattering.[4-7] For quasi-monochromatic probe radiation, the spectrally integrated scattering cross-section will be[8,9];

$$I_S(k) = \sigma_T(k) |f_i(k) + q(k)|^2 S_{ii}(k) ,$$

where, for elastic scattering, $k = 4\pi/\lambda \sin(\theta/2)$ is the scatter wave vector in the non-relativistic approximation, σ_T is the Thomson cross-section, f_i is the ionic form factor, accounting for scattering by core electrons, q represents the screening of the ion by free and valence electrons following the ion motion and S_{ii} is the ion-ion static structure factor.

S_{ii} is the Fourier transform of the radial pair distribution function, g(r), and is thus directly related to the microscopic structure of the material. This makes it a key parameter in determining other properties of the matter such as compressibility and conductivity.

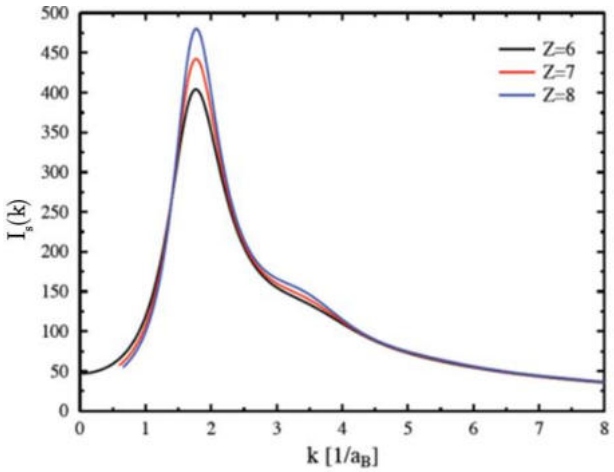

Figure 2. Simulations of total scattering cross section against the scatter wave vector k, in unis of the Bohr radius.

Figure 2 shows the expected scattering cross-section for iron at 2 eV, 10 g/cc and $Z^* = 6$-8. These simulations determine S_{ii} from calculating g(r) using the hypernetted chain approximation and a screened coulomb (Yukawa) potential between the ions. The scattering is especially sensitive to the inter-ionic potential at lower values of k (or scattering angle)[10].

Experimental Set-Up

An experiment was conducted in Target Area West (TAW) of the Vulcan laser facility. The six long pulse beams were

frequency doubled to 527nm using 12mm thick KDP crystals in type II configuration. Four beams were used to drive a shock wave though the sample target while the remaining two beams were utilised to produce a Titanium He_α ($1s^2$-1s2p ^1P transition) back lighter.

An optical streak camera (Hamamatsu C5680) recorded the temporal pulse profile on each data shot by monitoring leakage from one of the beams. All six beams were derived from the same seed pulse and were checked to have similar temporal profiles to each other earlier in the experiment. Typical pulse lengths were ~1-2ns. About 150 J of energy was available for generating the back lighter while about 300-400 J was available to generate the shock.

Targets were provided by CLF target fabrication staff, the sample target was a 7 μm iron layer coated with 6 μm of plastic (Paralene-N - C_8H_8). The sample target was irradiated by two pairs of beams, one pair at $\approx 45^0$ incidence, the other at $\approx 55^0$. Hybrid phase zone plates (HZP's) along with f/10 lenses were used to make a smooth, 1.2mm diameter, flat top focal spot, with intensities on target of ~ 10^{13} W/cm^2 (Figure 3). Scattering from the plastic layer can be treated as negligible due to the much lower number of bound electrons, especially as the CH will rapidly ionize, since $I_S \propto Z_b^2$ [11].

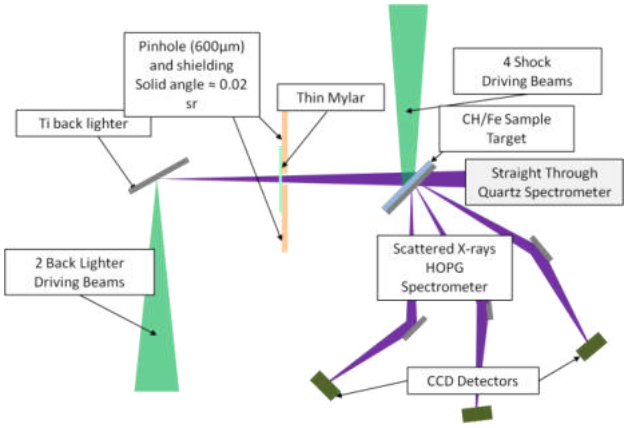

Figure 3. Experimental Set-Up

The X-ray back lighter was a 5 μm thick titanium target, irradiated by a pair of beams both incident at $\approx 30^0$ (figure 3),. These were focused to ~100μm; giving an intensity on target ~ 10^{15} W/cm^2. The conversion efficiency of incident laser energy into probe x-rays was about 0.1 %. The flux of probe x-rays onto the sample target was monitored using a flat quartz (10-12) crystal spectrometer.

The sample target was placed 6mm from the back lighter target. The projection of x-rays onto the sample was restricted to a cone of opening angle 0.2 rads by the use of a 600 μm pinhole in a 0.5 mm thick tantalum shield which was paced midway between the sample and back lighter, thus allowing only shocked material to be probed. This projection angle was chosen to match the collection angle of the crystals to give the optimal compromise between signal levels and angular resolution.

Scattered x-rays were collected by an array of three cylindrically bent highly orientated pyrolytic graphite (HOPG) crystals operating in Von Hamos geometry. These were coupled to *Andor* x-ray sensitive DX 420 back thinned CCD's set at normal incidence to the crystal center wavelength (2.61 Å). Two crystals were 30 mm (W) x 20 mm (L) with a 50 mm radius of curvature (r_c) while the third was 70 x 30 mm, r_c = 110 mm.

The back lighter driving beams could be delayed relative to the arrival of the shock driving beams by up to 4ns. This allowed probing of the WDM iron as it evolved.

The scatter diagnostics were shielded from back lighter direct emission by the tantalum. To verify that the signal observed was scattering from the sample and to quantify the scattering from cold iron and plastic a series of shots were taken; null, in which the back lighter target is irradiated with no sample in position; cold scatter, similar to a null but with a sample target in position; sample only, only the sample target is irradiated to give the background emission from the shock driving beams; and full, both a back lighter and sample target are in place and irradiated.

The optical streak camera was also used to monitor optical emission from the rear surface of the target. The leakage of B4 captured on the streak camera was used as a timing fiducial when the main pulse was incident on the sample target surface. Measurement of the delay between this fiducial pulse and emission from the rear surface of the sample target yielded the shock breakout time, and hence, average shock speed through the plastic/iron target. These measurements could not be taken during full shots so instead were taken as separate shots, referred to as shock breakout tests.

Experimental Results

Figure 4 shows the results of four shock breakout shots and the predicted result made by the 1-D radiative hydrodynamic simulation *HYADES* [12]. A 1-D simulation should be valid in this regime due to the high aspect ratio between target thickness and focal spot diameter[13]. The simulation used multi-group radiation transport, with 100 logarithmically spaced groups between 1eV and 15 keV and the *SESAME* equation of state tables, available from Los Alamos national laboratory [14]. The experimental shock breakout time is measured between the midpoint of the rising edges of the fiducial pulse and the sample rear surface emission; error bars are due to the combined effects of the streak camera resolution, determination of a suitable baseline and uncertainty in target thickness. Simulation results are the time between the midpoint of the rising edge of the incident laser pulse and when the final iron cell in the simulation rapidly increases in temperature; error bars are estimated by running separate simulations and varying factors such as laser intensity and pulse duration within the limits of experimental uncertainty.

Experiment and simulation were found to agree to within better than 5%. This gives confidence that *HYADES* will give reliable predictions of the experimental sample target conditions that will then be used as the input for simulations of the scattering.

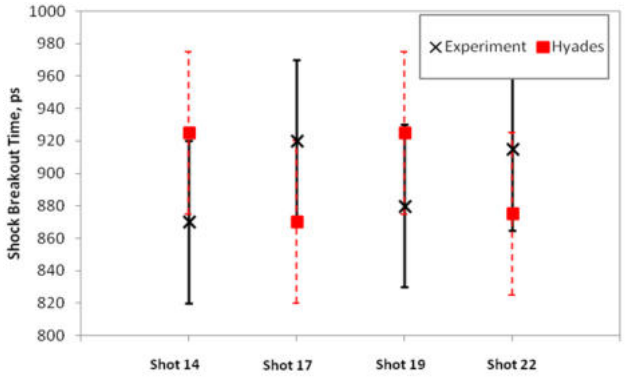

Figure 4. Comparison of measured shock breakout times and those predicted by Hyades.

Figure 5 shows the relative scattering intensity for a delay of 0.5ns. The results are the average of three shots taken under similar conditions. The error bars are the standard error in the mean. We have compared the data to a simulation of the total scattering using an HNC – Yukawa type approach. The conditions in the simulation were $Z^* = 6$, $T_e = 2$ eV and $\rho = 10$ g/cc.

We can see that the rise in the scattering cross-section predicted by the simulation agrees well with the experimental results. This suggests that indeed the scattering is sensitive to screening of the inter-ionic potential.

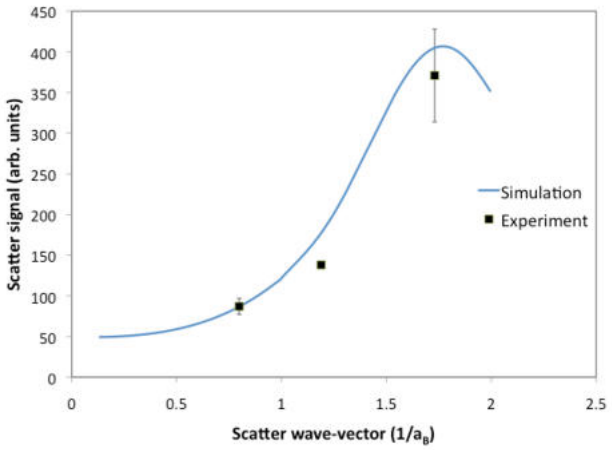

Figure 5. Comparison of experimental results with HNC simulation.

Conclusions

Suitable samples of WDM iron have been created using laser produced shocks and probed using x-ray scattering at 4.75 keV for the first time. Work to fully analyse the data is ongoing, but preliminary results show good agreement between measured and simulated values of the total scattering cross-sections and also provide some indication of the importance of inter-ionic screening.

Acknowledgements

The authors wish to acknowledge and thank the staff of the VULCAN laser, engineering, target area, and target fabrication at CLF for their help and support during the experiment.

This work was supported in part by EPSRC grant EP/G007462/1 and by the Science and Technology Facilities Council of the United Kingdom.

References

1. D.O. Gericke *et al, J. of Phys: Con. Series,* **220,** 012001 (2010)
2. D. Alfè *et al., Earth and Plan. Sci. Lett.* **195,** 91 (2002)
3. T. J. Aherns *et a.l, Geo. Phys. Lett.* **29,** 1150 (2002)
4. N. C. Woolsey, D. Riley, E. Nardi, *Rev. Sci. Inst.* **69,** 418 (1998).
5. D. Riley *et al., Phys. Rev. Lett.* **84,** 1704 (200)
6. S. H. Glenzer *et al., Phys. Rev. Lett.* **90,** 175002 (2003)
7. E. Garcia Saiz *et al, Nature Physiscs,* **4,** 940 (2008)
8. J. Chihara, *J. Phys. F: Met. Phys.* **17,** 295 (1987)
9. E. Nardi *et al., J. De. Physique*, **C7**, 267 (1988)
10. K. Wünsch *et al., Phys Rev. E,* **77,** 056404 (2008)
11. E. Garcia Saiz *et al, Phys. Rev. Letts.* **101,** 075003 (2008)
12. J. T. Larsen and S. M. Lane, *J. Quant. Spectrosc. Radiat. Transfer,* **51,** 179 (1994)
13. *The interaction of high power lasers with plasmas,* S. Eliezer, IoP Series in Plasma Physics, Inst. Of Physics Publishing, Bristol (2002).
14. S.P. Lyon and J. D. Johnson, Group T-1, Los Alamos National Laboratory Technical Report LA-UR-92E3407 (1992).